

Two-Dimensional Channel Parameter Estimation for Millimeter-Wave Systems Using Butler Matrices

Fazal-E-Asim¹, *Member, IEEE*, Felix Antreich², *Senior Member, IEEE*,
 Charles C. Cavalcante¹, *Senior Member, IEEE*, André L. F. de Almeida¹, *Senior Member, IEEE*,
 and Josef A. Nossek³, *Life Fellow, IEEE*

Abstract—In this paper, a novel two-dimensional parameter estimation method is proposed for frequency-selective millimeter-wave (mmWave) channels by probing a limited number of Kronecker products of discrete Fourier transform (DFT) beams, which are efficiently implemented in the analog domain by a novel combination of Butler matrices. The proposed strategy firstly estimates the channel parameters by using a modified parameter estimation via interpolation based on a DFT grid (PREIDG) algorithm. In a second step, high-resolution channel parameter estimation is achieved even in the low signal-to-noise-ratio (SNR) using the space-alternating generalized expectation-maximization (SAGE) algorithm. The proposed modified PREIDG algorithm outperforms state-of-the-art methods, e.g., the auxiliary beam pair (ABP) method while the SAGE algorithm achieves the derived Cramér-Rao lower bound (CRLB). Numerical results demonstrate that excellent estimation performance can be achieved for angle of departure (AoD) azimuth and elevation with addition to delay and complex path gain of each path even in the low SNR regime.

Index Terms—AoD estimation, Butler matrix, hybrid beamforming, millimeter wave, modified-PREIDG, space-alternating generalized expectation maximization, CRLB.

I. INTRODUCTION

THE next-generation of wireless communication systems promise to provide very high data rates for the user equipment (UE). To turn this dream into reality, one of the major competing candidates is the usage of mmWave spectrum with massive-multiple-input-multiple-output (MIMO) systems.

Manuscript received June 30, 2020; revised October 15, 2020; accepted December 4, 2020. Date of publication December 18, 2020; date of current version April 9, 2021. This work was supported in part by the Coordenação de Aperfeiçoamento de Pessoal de Nível Superior—Brasil (CAPES)—Finance Code 001 (Proc. 88882.183551/2018-01) and in part by the National Council of Scientific and Technological Development (CNPq) (Procs. 309472/2017-2 and 306616/2016-5). The associate editor coordinating the review of this article and approving it for publication was D. Matolak. (*Corresponding author: Fazal-E-Asim.*)

Fazal-E-Asim, Charles C. Cavalcante, and André L. F. de Almeida are with the Department of Teleinformatics Engineering, Federal University of Ceará, Fortaleza 60020-181, Brazil (e-mail: fazal asim@gtel.ufc.br; charles@gtel.ufc.br; andre@gtel.ufc.br).

Felix Antreich is with the Department of Telecommunications, Aeronautics Institute of Technology (ITA), São José dos Campos 12228-900, Brazil (e-mail: antreich@ieec.org).

Josef A. Nossek is with the Department of Teleinformatics Engineering, Federal University of Ceará, Fortaleza 60020-181, Brazil, and also with the Department of Electrical and Computer Engineering, Technical University of Munich, 80333 Munich, Germany (e-mail: josef.a.nossek@gtel.ufc.br).

Color versions of one or more figures in this article are available at <https://doi.org/10.1109/TWC.2020.3043958>.

Digital Object Identifier 10.1109/TWC.2020.3043958

The use of such high frequencies will facilitate the deployment of a large number of antennas both at the base station (BS) and the UE to achieve high beamforming gains [1], [2]. The large bandwidth available in the mmWave bands combined with a huge number of antenna elements both at the BS and UE poses a challenge for the hardware implementation of such a system [3]. Therefore, in addition to spectral efficiency, energy efficiency becomes a very important design goal.

The use of one radio-frequency (RF) chain per antenna is a very costly solution, so alternative solutions are proposed. One of the proposed solutions is the introduction of low resolution analog-to-digital converters (ADCs) [4]–[6] and another one is hybrid beamforming, where less RF chains are used to control a large number of antennas [7]–[10]. There are two main approaches of hybrid beamforming, namely, the fully connected analog phase shifting (FCAPS) network and the partially connected analog phase shifting (PCAPS) network. A FCAPS network has a high beamforming gain at the cost of less energy efficiency while a PCAPS network is more energy efficient but provides lower beamforming gain [11], [12]. A Butler matrix (BM) can be introduced in the analog domain to design the PCAPS network using fixed phase shifters (PSs) to avoid the implementation complexity of adaptive PSs. The works [13]–[15] showed the implementation of a BM to excite an uniform linear array (ULA) but no work has been published to excite a uniform rectangular array (URA) using Butler matrices (BMs).

On the one hand, a BM facilitates the energy-efficient and less complex implementation of hybrid beamforming. On the other hand achieving full capacity of the system becomes more challenging due to the limited number of fixed beams available. In this regard, [12] showed that taking into account hardware constraints and using a BM, we can still estimate the channel parameters efficiently considering a ULA. The work [16] analyzed the achievable rates using a DFT matrix, and assuming that the channel-state information (CSI) is perfectly known.

For wideband mmWave systems, the channels are frequency-selective, which complicates the channel parameter estimation task [17]–[19]. Recently, many techniques have been studied to solve the channel estimation problem in mmWave systems by exploiting the sparsity of the mmWave channel via compressed sensing (CS) tools [20]–[23]. An adaptive codebook is used for channel parameter

estimation based on CS considering a ULA [24], while in [25] an orthogonal matching pursuit (OMP) method is used to estimate the channel parameters. In [26], a frequency-selective scenario is considered assuming a hybrid architecture with quantized PSs and a CS-based approach is adopted for channel parameter estimation. Furthermore, a two-stage algorithm is introduced in [27], where the second stage is used for the refinement of the channel parameter estimates.

The authors in [28]–[31] proposed a beam pairing approach, therein referred to as ABP method, which is based on a set of many beam-pairs to estimate the corresponding AoDs. The authors showed that ABP outperforms the grid of beams (GoB) algorithm [32]. The work [11] showed that maximum likelihood (ML) channel estimation using BM can provide more accurate estimates than the ABP method for flat-fading channels.

In [33], the authors proposed a super-resolution parameter estimation algorithm for flat-fading channels, and showed that the ABP algorithm outperforms standard CS-based techniques like OMP [25] and the adaptive codebook method [24]. The authors in [34] proposed the use of high-resolution algorithms based on the estimation of signal parameters via rotational invariant techniques (ESPRIT), the so-called two-dimensional ESPRIT (TDE) and the minimum-searching algorithms for frequency-selective channels for uniform linear arrays, but both algorithms do not show good performance in the low SNR regime. Indeed, ESPRIT assumes a translation invariance of subarray responses and thus is more sensitive to array calibration errors [35], [36], while the SAGE algorithm is more resilient to model uncertainties caused by mutual coupling and sensor location errors [37]. Furthermore, it was demonstrated in [38]–[42] that SAGE outperforms multiple signal classification (MUSIC), unitary-ESPRIT and joint angle and delay estimation (JADE) algorithms.

The work in [43] is even extended the study to the coverage probability and handoff analysis with irregularly shaped cells. The authors in [44], proposed a closed-loop channel estimation by exploiting the sparsity in the angular and delay domains and using multi-dimensional unitary (MDU-ESPRIT). A low-rank tensor based channel estimation is proposed in [45], by applying CANDECOMP/PARAFAC (CP) decomposition into a third-order tensor to estimate the channel parameters from the associated factor matrices. Furthermore, the authors in [46], [47] proposed channel estimation based on an energy efficient analog implementation by introducing lens array, which avoids the implementation of a large number of active PSs, which may need high energy consumption. In addition, the lens array is used to shape the electromagnetic (EM) radiation, which is an interesting approach.

The performance of the SAGE algorithm comes at the cost of computational complexity. To overcome this issue, a more practical solution is proposed in [12], where a coarse estimation is achieved based on the PREIDG algorithm to initialize SAGE, which results in a drastic reduction of the computational complexity while maintaining the high-resolution performance for frequency-selective channels. Most of the aforementioned works are restricted to ULAs, while our interest in on URAs using two-dimensional BMs that can

operate on azimuth and elevation dimensions by exploiting their inherent Kronecker factorization structure.

In this paper, we propose a novel two-dimensional parameter estimation method for frequency-selective mmWave channels by probing a limited number of Kronecker products of DFT beams, which are efficiently implemented in the analog domain by a novel combination of Butler matrices. This limits the pilot overhead but leaves a challenging problem, i.e., to improve the channel capacity with these available limited beams. The problem is tackled by means of a novel two-stage combination of BMs for energy-efficient implementation of the PCAPS network to excite an URA and to achieve two-dimensional channel parameter estimation for frequency-selective channels. To ensure high-resolution parameter estimation with low complexity, we propose a two-step approach. Firstly, a coarse estimation of the channel parameters is carried out using a modified PREIDG algorithm. Note that, the coarse estimation with PREIDG from [12], which interpolates between the DFT spatial frequencies in one angular dimension will be extended to two angular dimensions using modified PREIDG. These coarse estimates are used to initialize a SAGE-based algorithm that provides high-resolution estimates of path delays, angles and gains, even in the low SNR regime. Our results demonstrate remarkable performance of the proposed method, which outperforms the state-of-the-art ABP method. The contributions of this work are summarized as follows:

- We propose a novel strategy to excite the URA structures using multiple BMs, which provides an energy-efficient implementation with fixed PSs.
- To ensure a high-resolution channel parameter estimation using the SAGE algorithm with less computational complexity, a novel modified PREIDG estimation algorithm is proposed to initialize SAGE.
- The proposed initialization with the modified PREIDG algorithm provides model order estimation and enables robust initialization of the subsequent high-resolution parameter estimation stage using SAGE which reaches convergence with only a few iterations.
- We derive new expressions of the SAGE algorithm for the problem at hand, and also provide the analytical expressions for the CRLB considering a multi-user (MU)-multiple-input-single-output (MISO) system where the BS is equipped with an URA and the UEs have a single antenna.

Notation: a (lower case italic letters) denote scalars, \mathbf{a} (bold lowercase letters) denote vectors and \mathbf{A} (bold upper case letters) denote matrices; \mathbf{I}_M represents identity matrix of size $M \times M$; $\mathbf{1}_M$ denote all ones matrix of $M \times M$ dimensions; $\mathbf{1}_{M \times N}$ is all ones matrix of size $M \times N$; entry of \mathbf{A} at the p th row and q th column is represented as $[\mathbf{A}]_{p,q}$; $\max(\mathbf{a})$ gives the index of the maximum value in the vector \mathbf{a} ; \odot represents Hadamard product; \otimes represents Kronecker product; $(\cdot)^H$ represents conjugate transpose; $\mathbb{E}\{\cdot\}$ represents expectation; $\lfloor \cdot \rfloor$ represents floor operator; $\text{unvec}\{\mathbf{a}\}$ and $\text{diag}\{\mathbf{a}\}$ represents un-vectorization of \mathbf{a} and the square diagonal matrix with elements of vector \mathbf{a} across

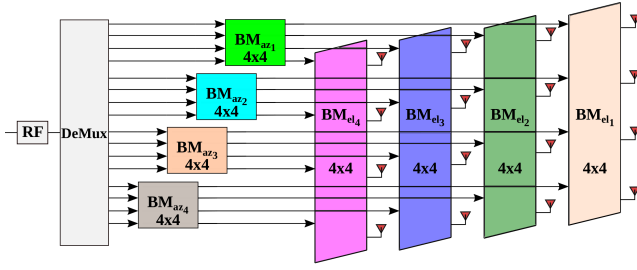


Fig. 1. An architecture of Butler matrices exciting a two-dimensional URA (one-subarray) with $M = M_h M_v = 16$.

the main diagonal; $\text{tr}\{\cdot\}$ represents trace of the matrix and $\text{mod}(\cdot)$ represents modulus, respectively.

II. SYSTEM MODEL

A. System Architecture

To realize two-dimensional beamforming for the next-generation mobile communication systems, an URA is introduced which simplifies multiuser spatial separation in a cell while maximizing the available data rates and minimizing the inter-user interference. Employing large antennas at the BS is a challenge that can be tackled by introducing hybrid beamforming with a PCAPS network using BMs in the analog domain to ensure an energy efficient implementation [11], [12], [48]. The idea is to extend the ULA excited by a single BM as discussed in [11], [12] to a two-dimensional URA, which is of more practical interest. As explained in detail in [11], [12], that the BM is the analog-RF implementation of the DFT matrix, which is constructed using multiple 90° hybrids with few fixed PSs implemented with a piece of transmission line, and used to excite ULA. To excite URA in a similar fashion, we propose a new way of combining BMs as shown in Fig. 1. The new thing in Fig. 1 is to devise an architecture with BMs that is matched to URAs, therefore the layout in Fig. 1 is just an example of an exciting one subarray, driven by one RF-chain. In this two-dimensional network of BMs, the resultant beamforming vector is the Kronecker product of the columns of DFT matrices as

$$\mathbf{w}(\delta_p, \nu_q) = \mathbf{w}_h(\delta_p) \otimes \mathbf{w}_v(\nu_q) \in \mathbb{C}^{M \times 1}, \quad (1)$$

where $\mathbf{w}(\delta_p, \nu_q)$ is the resultant beamforming vector for probing the channel, δ_p is the DFT spatial frequency of the DFT matrix controlling the horizontal antenna elements, and $\mathbf{w}_h(\delta_p)$ is defined as

$$\mathbf{w}_h(\delta_p) = \frac{1}{\sqrt{M_h}} \left[1, e^{-j\delta_p}, \dots, e^{-j(M_h-1)\delta_p} \right]^T \in \mathbb{C}^{M_h \times 1}, \quad (2)$$

where $\delta_p = \frac{2\pi}{M_h} p$, $p = 0, \dots, M_h - 1$. M_h is the number of antenna elements on the horizontal axis, and ν_q is the DFT spatial frequency of the BM exciting the vertical antenna elements in the URA, while $\mathbf{w}_v(\nu_q)$ is defined as

$$\mathbf{w}_v(\nu_q) = \frac{1}{\sqrt{M_v}} \left[1, e^{-j\nu_q}, \dots, e^{-j(M_v-1)\nu_q} \right]^T \in \mathbb{C}^{M_v \times 1}, \quad (3)$$

where $\nu_q = \frac{2\pi}{M_v} q$, $q = 0, \dots, M_v - 1$, and M_v is the number of antenna elements on the vertical axis.

B. Signal Model

We consider a single-cell downlink scenario for a frequency selective channel, where the BS is equipped with N antennas, and there may be a number of UEs having single antenna each. The BS employs a PCAPS network [11], [12], where each sub-array is composed of M antennas satisfying $N = MN_{RF}$, controlled by N_{RF} chains. The two-dimensional beamforming vector $\mathbf{w}(\delta_p, \nu_q)$ is used to probe the channel with a specific constant amplitude zero autocorrelation (CAZAC) [49]–[51] sequence. By assuming the number of antennas in each subarray M equals to the length of the CAZAC sequence L , i.e., $L = M$ leads to generation of QPSK symbols, which is constant modulus and enable to drive the power amplifier (PA) near saturation. The resulting received vector of one single antenna UE, i.e., $\mathbf{y}_m \in \mathbb{C}^{L \times 1}$ per one sub-array is given as

$$\mathbf{y}_m^T = \sqrt{P_T} \sum_{r=1}^R \alpha_r \mathbf{a}^H(\phi_r, \theta_r) \mathbf{w}_m(\delta_p, \nu_q) \mathbf{c}_m^T(\tau_r) + \mathbf{n}_m^T, \quad (4)$$

where m is specifying, which beamforming vector and CAZAC sequence has been used and is given as, $m = q + (p-1)M_v$, $q \in \{1, \dots, M_v\}$, $p \in \{1, \dots, M_h\}$, and $m \in \{1, \dots, M_h M_v = M\}$. P_T is the transmit power, α_r is the complex gain of each path r , \mathbf{c}_m is the specific CAZAC sequence of length L having a one-to-one correspondence with the two-dimensional beamforming vector $\mathbf{w}_m(\delta_p, \nu_q)$, $\mathbf{n}_m \sim \mathcal{CN}(\mathbf{0}_{L \times 1}, \sigma_n^2 \mathbf{I}_L)$ is the noise vector, σ_n^2 is the noise variance, ϕ_r is the azimuth AoD, θ_r is the elevation AoD, and $\mathbf{a}(\phi_r, \theta_r)$ is the two-dimensional steering vector of a URA in the y - z -plane having inter-antenna element spacing across the horizontal and vertical axes as $d_h = d_v = \lambda/2$, therefore the array element response is given as

$$a_m(\phi_r, \theta_r) = e^{-j\pi[(p-1)\sin\theta_r \sin\phi_r + (q-1)\cos\theta_r]}, \quad (5)$$

where $m = 1, \dots, M$. The URA has M_h antenna elements in the y direction and M_v elements in the z direction, with $M = M_h M_v$, as shown in Fig. 2.

Now, let us consider the two-dimensional steering vector $\mathbf{a}(\phi_r, \theta_r)$ given in (5) and define the spatial frequencies as $\mu_r = \pi \sin\theta_r \sin\phi_r$ and $\psi_r = \pi \cos\theta_r$ respectively. Therefore, the steering vector can be re-written as

$$\mathbf{a}(\mu_r, \psi_r) = [a_1(\mu_r, \psi_r), a_2(\mu_r, \psi_r), \dots, a_M(\mu_r, \psi_r)]^T, \quad (6)$$

where

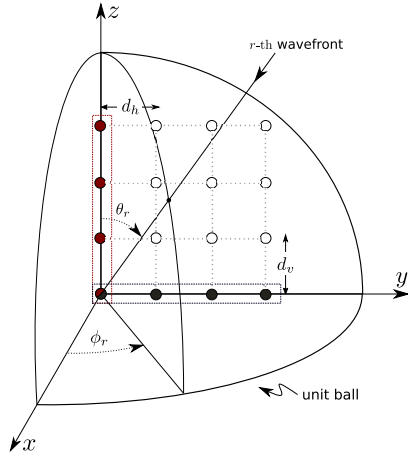
$$a_m(\mu_r, \psi_r) = e^{-j\pi[(p-1)\mu_r + (q-1)\psi_r]}. \quad (7)$$

Furthermore, (6) can also be re-written as the Kronecker product between the following steering vectors

$$\mathbf{a}_h(\mu_r) = [1, e^{-j\mu_r}, \dots, e^{-j(M_h-1)\mu_r}]^T \in \mathbb{C}^{M_h \times 1}, \quad (8)$$

and

$$\mathbf{a}_v(\psi_r) = [1, e^{-j\psi_r}, \dots, e^{-j(M_v-1)\psi_r}]^T \in \mathbb{C}^{M_v \times 1}. \quad (9)$$

Fig. 2. Uniform rectangular array in y - z -plane.

Hence, the channel steering vector $\mathbf{a}(\mu_r, \psi_r)$ can also be written as

$$\mathbf{a}(\mu_r, \psi_r) = \mathbf{a}_h(\mu_r) \otimes \mathbf{a}_v(\psi_r) \in \mathbb{C}^{M \times 1}. \quad (10)$$

The CAZAC sequence specific for each beamforming vector is \mathbf{c}_m , where each symbol is constructed as

$$c(n) = e^{j \frac{2\pi}{\sqrt{L}} (\text{mod}\{n, \sqrt{L}\} + 1) (\lfloor \frac{n}{\sqrt{L}} \rfloor + 1) + j \frac{\pi}{4}}, \quad (11)$$

and $n \in \{0, 1, \dots, L-1\}$. The CAZAC sequence for the first beamforming vector is given as

$$\mathbf{c}_1(0) = [c(0), c(1), \dots, c(L-1)]^T \in \mathbb{C}^{L \times 1} \quad (12)$$

$\mathbf{c}_m(0)$, where $m = 1, \dots, M_h M_v = M$ are shifted versions of $\mathbf{c}_1(0)$ and assigned each wrap around to a specific beamforming vector.

By probing all the two-dimensional beamforming vectors with their specific CAZAC sequences in a round-robin fashion and collecting all the receive vectors \mathbf{y}_m in the matrix $\mathbf{Y} \in \mathbb{C}^{M \times L}$ leads to

$$\mathbf{Y} = \begin{bmatrix} \mathbf{y}_1^T \\ \mathbf{y}_2^T \\ \vdots \\ \mathbf{y}_M^T \end{bmatrix} = \sqrt{P_T} \sum_{r=1}^R \alpha_r \mathbf{A}(\mu_r, \psi_r, \delta_p, \nu_q) \times \underbrace{\begin{bmatrix} \mathbf{c}_1^T(\tau_r) \\ \mathbf{c}_2^T(\tau_r) \\ \vdots \\ \mathbf{c}_M^T(\tau_r) \end{bmatrix}}_{=\mathbf{C}(\tau_r)} + \underbrace{\begin{bmatrix} \mathbf{n}_1^T \\ \mathbf{n}_2^T \\ \vdots \\ \mathbf{n}_M^T \end{bmatrix}}_{=\mathbf{N}}, \quad (13)$$

which can be compactly written as

$$\mathbf{Y} = \sqrt{P_T} \sum_{r=1}^R \alpha_r \mathbf{A}(\mu_r, \psi_r, \delta_p, \nu_q) \mathbf{C}(\tau_r) + \mathbf{N}, \quad (14)$$

where $\mathbf{A}(\mu_r, \psi_r, \delta_p, \nu_q) \in \mathbb{C}^{M \times M}$ is given by

$$\mathbf{A}(\mu_r, \psi_r, \delta_p, \nu_q) = \text{diag} \left\{ \mathbf{a}^H(\mu_r, \psi_r) \mathbf{w}_m(\delta_p, \nu_q) \right\}_{m=1}^{M=M_h M_v}, \quad (15)$$

and the noise covariance matrix is

$$\mathbf{R} = \mathbb{E} [\text{vec}\{\mathbf{N}\} \text{vec}\{\mathbf{N}\}^H] = \sigma_n^2 \mathbf{I}_{ML}, \quad (16)$$

assuming spatially and temporally uncorrelated noise.

III. COARSE ESTIMATION BASED ON MODIFIED PREIDG

In the two-stage estimation algorithm, the first stage is responsible for estimating the model order and the channel parameters which are achieved by the modified PREIDG. We use M CAZAC sequences of length $L = M$ having a one-to-one correspondence to M two-dimensional beamforming vectors which are used to probe the channel. This means that each UE observes M consecutive sequences \mathbf{y}_m (4) and the received signals are multiplied with stored CAZAC sequences \mathbf{c}_m^* , and can be formulated for one UE as

$$\mathbf{Z} = \mathbf{Y} \mathbf{C}^H(0) = \sqrt{P_T} \sum_{r=1}^R \alpha_r \mathbf{A}(\mu_r, \psi_r, \delta_p, \nu_q) \times \mathbf{C}(\tau_r) \mathbf{C}^H(0) + \mathbf{N} \mathbf{C}^H(0), \quad (17)$$

where $\mathbf{C}(0) \in \mathbb{C}^{M \times L}$ is the CAZAC sequences matrix with time-delay equal to zero. The post-correlation power matrix \mathbf{P} can be given as

$$\mathbf{P} = \mathbb{E} [\mathbf{Z} \odot \mathbf{Z}^*]. \quad (18)$$

Now, in a real scenario, the matrix \mathbf{P} will not be sparse but can provide useful information about the model order, i.e., the number of multipaths, and the channel parameters such as $\sqrt{P_T}$, α_r , ψ_r , μ_r and τ_r of each path. We exploit the power matrix by searching the (wrap-around) diagonals

$$\mathbf{p}_{i_r}^T = [p_{1,i}, p_{2, \text{mod}(i, M)+1}, \dots, p_{M, \text{mod}(i+M-2, M)+1}]^T \in \mathbb{R}^M, \quad (19)$$

where $i = 1, \dots, M$, with \mathbf{p}_1 being the main diagonal of \mathbf{P} in (18). For each diagonal \mathbf{p}_{i_r} , we check, whether the largest element is above a certain threshold G as follows,

$$\max_{k=1, \dots, M} (p_{k, \text{mod}(i+(k-2), M)+1}) \geq G, \quad i = 1, \dots, M. \quad (20)$$

G should be chosen heuristically such that we can detect signals above the noise floor $\sigma_n^2 M$. Note that, the choice of threshold has an influence on the estimation of model order, i.e., the number of multipaths R . Choosing G to high or to low, the model order may be underestimated or overestimated. The intuitive logic behind this heuristic hard threshold G is that the multipath should exceed from this threshold, otherwise we assume that it is weak due to the high path-loss, and is not worthwhile to estimate it. The integer delay τ_{i_r} for the r th path can be found as

$$\hat{\tau}_{i_r} = i_r - 1. \quad (21)$$

For the main diagonal \mathbf{p}_1 , this will always be fulfilled assuming a line-of-sight (LOS) path, which has relative delay $\tau_i = i_1 - 1|_{i_1=1} = 0$. The number of diagonals \mathbf{p}_i , fulfilling (20) is the estimated model order \hat{R} and provides a coarse estimate $\hat{\tau}_{i_r}$ for each path. For notational convenience, the index r in the estimated integer delay $\hat{\tau}_{i_r}$ is dropped in the next sections.

A. Look-Up Table (LUT)

To get the coarse estimates of the spatial frequencies $\hat{\mu}_r$ and $\hat{\psi}_r$, we design only one LUT, which will be used for both the azimuth beamforming angles δ_p and the elevation beamforming angles ν_q . We show this in detail for $\hat{\mu}_r$, where we use linear interpolation with $D + 1$ spatial frequencies μ_d given as

$$\mu_d = \delta_p + d\Delta_\mu, \quad d = 0, \dots, D, \quad (22)$$

with

$$\Delta_\mu = \frac{\delta_{p+1} - \delta_p}{D} = \frac{2\pi}{M_h D}. \quad (23)$$

Now, considering the two successive azimuth spatial frequencies δ_p and δ_{p+1} , we compute the noise-free normalized power measure using a hypothetical spatial frequency μ_d as

$$P_{p,d} = |\mathbf{a}_h^H(\mu_d)\mathbf{w}_h(\delta_p)|^2, \quad (24)$$

and

$$P_{p+1,d} = |\mathbf{a}_h^H(\mu_d)\mathbf{w}_h(\delta_{p+1})|^2, \quad (25)$$

where the channel steering vector for a hypothetical spatial frequency μ_d is given as

$$\mathbf{a}_h(\mu_d) = [1, e^{-j\mu_d}, \dots, e^{-j(M_h-1)\mu_d}]^T \in \mathbb{C}^{M_h \times 1}. \quad (26)$$

The ratio between the two power measures $P_{p,d}$ and $P_{p+1,d}$ is defined as,

$$\Delta_d = \sqrt{\frac{P_{p,d}}{P_{p+1,d}}}. \quad (27)$$

Note that the power measures $P_{p,d}$ and $P_{p+1,d}$ can be taken for any spatial frequency pair $\{\delta_p, \delta_{p+1}\}$ regardless of its specific value, as long as they fall on the DFT grid. Otherwise stated, $P_{p,d}$ and $P_{p+1,d}$ are independent of p . Note that, to fill the LUT, we only need $D + 1$ ratios according to (27). Moreover, once we generate the LUT for the estimation of the azimuth spatial frequency μ_r , it can be reused for the estimation of the elevation spatial frequency ψ_r .

B. Estimation of Spatial Frequencies

Once the model order \hat{R} is determined, the spatial frequencies should be estimated. Note that $\mathbf{p}_{i_r} \in \mathbb{C}^{M \times 1}$ is the diagonal or cross diagonal vector of the received power matrix $\mathbf{P} \in \mathbb{C}^{M \times L}$ for the r th path as defined in (19), where $M_h M_v = M$. Unvectorizing the selected \mathbf{p}_{i_r} yields

$$\mathbf{P}'_r = \text{unvec}\{\mathbf{p}_{i_r}\}^T \in \mathbb{C}^{M_h \times M_v}. \quad (28)$$

Now, each entry of \mathbf{P}'_r is assigned to the corresponding beamforming vector $\mathbf{w}(\delta_p, \nu_q)$. We see that $[\mathbf{P}'_r]_{p,q}^{\max}$ as shown in Fig. 3, i.e., the entry in the p th row and q th column of \mathbf{P}'_r has been generated by the following beamforming vector,

$$\mathbf{w}(\delta_{p-1}, \nu_{q-1}) = \mathbf{w}_h(\delta_{p-1}) \otimes \mathbf{w}_v(\nu_{q-1}). \quad (29)$$

Assuming that the second largest entry in the p th row is $[\mathbf{P}'_r]_{p,q-1}$ and in the q th column is $[\mathbf{P}'_r]_{p+1,q}$, the interpolation

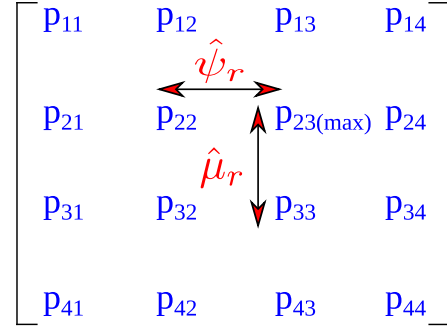


Fig. 3. Two-dimensional power-matrix \mathbf{P}'_r for estimation of spatial frequencies $\hat{\mu}_r$ and $\hat{\psi}_r$.

for μ_r should be carried out between $\delta_{p-1} < \hat{\mu}_r < \delta_p$ and for ψ_r between $\nu_{q-2} < \hat{\psi}_r < \nu_{q-1}$.

Now let us use the LUT constructed according to (22)-(27) and let us choose those indices d and $d + 1$ such that Δ_d and Δ_{d+1} are the two ratios closest to

$$\Delta_{\mu_r} = \sqrt{\frac{[\mathbf{P}'_r]_{p,q}}{[\mathbf{P}'_r]_{p+1,q}}}. \quad (30)$$

We estimate μ_r as

$$\hat{\mu}_r = \mu_d + b_\mu \Delta_\mu, \quad (31)$$

with

$$b_\mu = \frac{\Delta_d - \Delta_{\mu_r}}{\Delta_d - \Delta_{d+1}}. \quad (32)$$

The μ_r estimation approach is given in Algorithm 1. The same procedure is used to estimate $\hat{\psi}_r$.

Algorithm 1 Two-Dimensional Parameter Estimation of $\hat{\mu}_r$ Based on Modified PREIDG

Require: $\mathbf{Y}(13)$;

- 1: Determine \mathbf{p}_{i_r} from (18) and (19);
 - 2: Rearrange \mathbf{p}_{i_r} in the power matrix \mathbf{P}'_r as shown in (28);
 - 3: Find the highest power $[\mathbf{P}'_r]_{p,q}^{\max}$ and the associated beamforming vector $\mathbf{w}(\delta_{p-1}, \nu_{q-1})$;
 - 4: Find the second highest power in the q th column $[\mathbf{P}'_r]_{p+1,q}$ and the associated $\mathbf{w}(\delta_p, \nu_{q-1})$;
 - 5: Calculate Δ_{μ_r} as in (30);
 - 6: Find d such that $\Delta_d \geq \Delta_{\mu_r} \geq \Delta_{d+1}$ as in (27);
 - 7: Calculate constant b_μ as in (32);
 - 8: **Return** $\hat{\mu}_r$ as in (31).
-

C. Example With a 4×4 URA

Let us take a 4×4 URA having $M_h = 4$ and $M_v = 4$. The horizontal and vertical beamforming vectors are given by

$$\mathbf{w}_h(\delta_p) = \frac{1}{2} [1, e^{-j\delta_p}, e^{-j2\delta_p}, e^{-j3\delta_p}]^T, \quad (33)$$

and

$$\mathbf{w}_v(\nu_q) = \frac{1}{2} [1, e^{-j\nu_q}, e^{-j2\nu_q}, e^{-j3\nu_q}]^T, \quad (34)$$

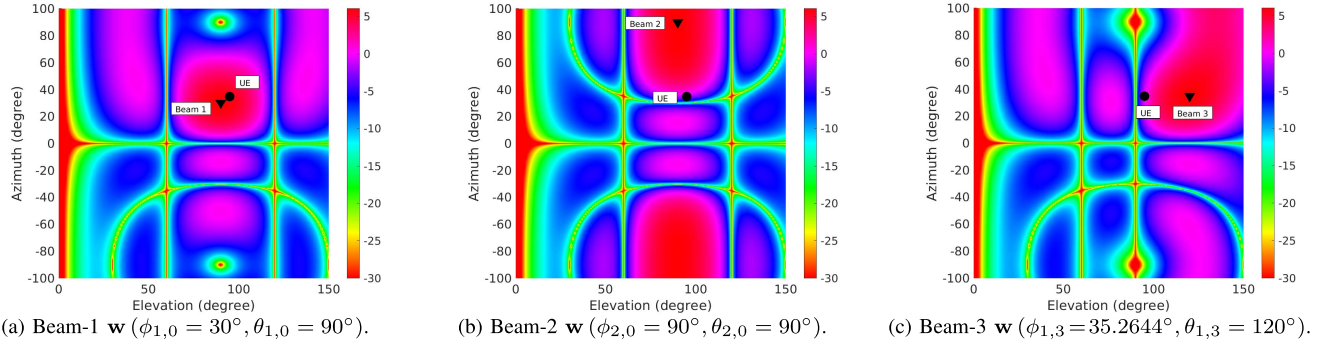


Fig. 4. An example of two-dimensional parameter estimation via modified PREIDG for UE ($\phi = 35^\circ, \theta = 95^\circ$).

where $\delta_0 = \nu_0 = 0$, $\delta_1 = \nu_1 = \frac{\pi}{2}$, $\delta_2 = \nu_2 = \pi$, $\delta_3 = \nu_3 = \frac{3\pi}{2}$. The resultant two-dimensional beamforming vector can be written as

$$\begin{aligned} \mathbf{w}(\delta_p, \nu_q) &= \mathbf{w}(\delta_p) \otimes \mathbf{w}(\nu_q) \\ &= \frac{1}{4} \left[1, e^{-j\nu_q}, e^{-j2\nu_q}, e^{-j3\nu_q}, e^{-j\delta_p}, e^{-j(\delta_p+\nu_q)}, e^{-j(\delta_p+2\nu_q)}, \right. \\ &\quad \left. e^{-j(\delta_p+3\nu_q)}, \dots, e^{-j(3\delta_p+2\nu_q)}, e^{-j(3\delta_p+3\nu_q)} \right]^T. \end{aligned} \quad (35)$$

When generating the power matrix \mathbf{P} in (18), each row is obtained with one beamforming vector $\mathbf{w}(\delta_p, \nu_q)$, i.e., with one index pair (p, q) .

Let us assume that the r th path has an integer-delay $\tau_{i_r} = i_r - 1 = 5$. The diagonal \mathbf{p}_{i_r} looks as follows:

$$\mathbf{p}_{i_r} = [\mathbf{P}_{11}, \dots, \mathbf{P}_{14}, \mathbf{P}_{21}, \dots, \mathbf{P}_{24}, \mathbf{P}_{31}, \dots, \mathbf{P}_{34}, \mathbf{P}_{41}, \dots, \mathbf{P}_{44}]^T, \quad (36)$$

and

$$\mathbf{P}'_r = \text{unvec}\{\mathbf{p}_{i_r}\}^T = \begin{bmatrix} \mathbf{P}_{11} & \mathbf{P}_{12} & \mathbf{P}_{13} & \mathbf{P}_{14} \\ \mathbf{P}_{21} & \mathbf{P}_{22} & \mathbf{P}_{23} & \mathbf{P}_{24} \\ \mathbf{P}_{31} & \mathbf{P}_{32} & \mathbf{P}_{33} & \mathbf{P}_{34} \\ \mathbf{P}_{41} & \mathbf{P}_{42} & \mathbf{P}_{43} & \mathbf{P}_{44} \end{bmatrix}. \quad (37)$$

Therefore, the power entry $[\mathbf{P}'_r]_{p,q}$ has been produced with $\mathbf{w}(\delta_{p-1}, \nu_{q-1})$. At the UE side, let us assume azimuth and elevation angles given by $\phi = 35^\circ$ and $\theta = 95^\circ$, respectively, as shown in Fig. 4. The three beamforming vectors should be

- Beam 1 : $\mathbf{w}(\delta_1, \nu_0)$ with $\phi_{1,0} = 30^\circ, \theta_{1,0} = 90^\circ$
- Beam 2 : $\mathbf{w}(\delta_2, \nu_0)$ with $\phi_{2,0} = 90^\circ, \theta_{2,0} = 90^\circ$
- Beam 3 : $\mathbf{w}(\delta_1, \nu_3)$ with $\phi_{1,3} = 35.2644^\circ, \theta_{1,3} = 120^\circ$.

The corresponding positions in the \mathbf{P}'_r matrix are

$$\begin{aligned} \text{Beam 1 : } & [\mathbf{P}'_r]_{2,1} = [\mathbf{P}'_r]_{2,1}^{\max} \\ \text{Beam 2 : } & [\mathbf{P}'_r]_{3,1} \\ \text{Beam 3 : } & [\mathbf{P}'_r]_{2,4}. \end{aligned}$$

Therefore, the interpolation for $\hat{\mu}_r$ should take place between δ_1 and δ_2 which correspond to beam 1 and beam 2, respectively. Similarly, the interpolation for $\hat{\psi}_r$ should take place between ν_3 and ν_0 , which correspond to beam 3 and beam 1, respectively.

Since δ_p and ν_q in the DFT matrices are in the range $[0, 2\pi)$, and Algorithm 1 considers them in the range $(-\pi, \pi]$, the following transformation is applied:

$$x = \text{mod}(x + \pi, 2\pi) - \pi, \quad x \in \{\delta_p, \nu_q, \hat{\mu}_r, \hat{\psi}_r\}. \quad (38)$$

Finally, we can extract an estimate of $\hat{\phi}_r$ and $\hat{\theta}_r$ as

$$\hat{\theta}_r = \arccos\left(\frac{\hat{\psi}_r}{\pi}\right), \quad (39)$$

$$\hat{\phi}_r = \arcsin\left(\frac{\hat{\mu}_r}{\pi \sin(\hat{\theta}_r)}\right), \quad (40)$$

with the range of $\theta_r^\circ \sim \text{U}(90^\circ, 130^\circ)$ and $\phi_r^\circ \sim \text{U}(-60^\circ, 60^\circ)$.

Remark: The interpolation between δ_{p-1} and δ_p for estimating μ_r , and similarly the interpolation between ν_{q-2} and ν_{q-1} for estimating ψ_r can go wrong in some cases, especially if the signal level is weak. For instance, let us suppose that μ_r is close to the δ_{p-1} with the highest power, but the received power generated using δ_p may be close to the noise floor. Likewise, suppose that ψ_r is close to ν_{q-1} with highest received power but the received power generated using ν_{q-2} may be close to the noise floor. In this case, we can adopt the following checking procedure

$$\begin{cases} |[\mathbf{P}'_r]_{p,q+1} - [\mathbf{P}'_r]_{p,q-1}| \leq \sigma_n^2, \\ |[\mathbf{P}'_r]_{p+1,q} - [\mathbf{P}'_r]_{p-1,q}| \leq \sigma_n^2. \end{cases} \quad (41)$$

If (41) is fulfilled, then it is not worthwhile to interpolate at all, but simply choose $\hat{\mu}_r = \delta_{p-1}$, and $\hat{\psi}_r = \nu_{q-1}$.

IV. HIGH-RESOLUTION CHANNEL PARAMETER ESTIMATION USING SAGE

High-resolution channel parameter estimation plays an important role in designing hybrid precoders at the BS because the channel parameters need to be quantized before being sent back to the BS. In practice, the BS receives the channel parameters with quantization errors resulting in deterioration of the performance. This deterioration can be increased if the channel parameters are not estimated with high accuracy.

It is known in the literature that SAGE and ESPRIT are high-resolution estimation algorithms [52], but the SAGE algorithm can provide the highest accuracy as compared to MUSIC and ESPRIT [38]. On the other hand, ESPRIT has less

complexity than the standard SAGE algorithm, but requires two translation invariant subarrays in the URA while on the other hand SAGE does not impose such kind of restriction.

To ensure a high-resolution parameter estimation at a lower complexity, we initialize the SAGE algorithm with coarse estimates achieved by the modified PREIDG algorithm. We use the fundamental principles of the SAGE algorithm [53], [54] to derive new expressions for our non-linear problem at hand. This solution yields a refined estimate of the complex path gains and non-integer delays, as will be shown in our results.

Let us assume that \mathbf{Y} in (13) follows a multivariate complex Gaussian probability density function (pdf) which is parameterized by the unknown channel parameter vector $\boldsymbol{\eta}$ as

$$\boldsymbol{\eta} = \left[\sqrt{P_T} \text{Re}\{\boldsymbol{\alpha}\}^T, \sqrt{P_T} \text{Im}\{\boldsymbol{\alpha}\}^T, \boldsymbol{\mu}^T, \boldsymbol{\psi}^T, \boldsymbol{\tau}^T \right]^T, \quad (42)$$

where

$$\sqrt{P_T} \text{Re}\{\boldsymbol{\alpha}\} = \left[\sqrt{P_T} \text{Re}\{\alpha_1\}, \dots, \sqrt{P_T} \text{Re}\{\alpha_R\} \right]^T \in \mathbb{C}^{R \times 1}, \quad (43)$$

$$\sqrt{P_T} \text{Im}\{\boldsymbol{\alpha}\} = \left[\sqrt{P_T} \text{Im}\{\alpha_1\}, \dots, \sqrt{P_T} \text{Im}\{\alpha_R\} \right]^T \in \mathbb{C}^{R \times 1}, \quad (44)$$

$$\boldsymbol{\mu} = [\mu_1, \dots, \mu_R]^T \in \mathbb{C}^{R \times 1}, \quad (45)$$

$$\boldsymbol{\psi} = [\psi_1, \dots, \psi_R]^T \in \mathbb{C}^{R \times 1}, \quad (46)$$

$$\boldsymbol{\tau} = [\tau_1, \dots, \tau_R]^T \in \mathbb{C}^{R \times 1}. \quad (47)$$

Thus, the likelihood can be given as

$$\begin{aligned} L(\mathbf{Y}; \boldsymbol{\eta}) &= \frac{1}{\pi^{ML} \det \mathbf{R}} \\ &\times \exp \left(-\text{vec} \left\{ \mathbf{Y} - \sqrt{P_T} \sum_{r=1}^R \alpha_r \mathbf{A}(\mu_r, \psi_r, \delta_p, \nu_q) \mathbf{C}(\tau_r) \right\}^H \right. \\ &\times \left. \mathbf{R}^{-1} \text{vec} \left\{ \mathbf{Y} - \sqrt{P_T} \sum_{r=1}^R \alpha_r \mathbf{A}(\mu_r, \psi_r, \delta_p, \nu_q) \mathbf{C}(\tau_r) \right\} \right). \end{aligned} \quad (48)$$

The expectation step estimates the hidden data space as

$$\begin{aligned} \hat{\mathbf{X}}_r &= \mathbb{E}_{\mathbf{X}_r}[\mathbf{X}_r | \mathbf{Y}; \hat{\boldsymbol{\eta}}] \\ &= (1 - \beta_r) \mathbf{S}_r(\hat{\boldsymbol{\eta}}_r) + \beta_r \left(\mathbf{Y} - \sum_{\substack{r'=1 \\ r' \neq r}}^R \mathbf{S}_{r'}(\hat{\boldsymbol{\eta}}_{r'}) \right), \end{aligned} \quad (49)$$

where, the parameter β_r controls the rate of convergence of the SAGE algorithm. For $\beta_r = 0$ the estimate of the hidden data space \mathbf{X}_r is not updated, for $\beta_r = 1$ the rate of convergence is largest due to the amount of new information incorporated into the estimate of the hidden data space. Thus, choosing $\beta_r = 1$ speeds up convergence of the SAGE algorithm and also minimizes the number of iterations needed to converge to the global optimum. Therefore, by choosing $\beta_r = 1$, we have

$$\hat{\mathbf{X}}_r = \mathbf{Y} - \sum_{\substack{r'=1 \\ r' \neq r}}^R \mathbf{S}_{r'}(\hat{\boldsymbol{\eta}}_{r'}) \in \mathbb{C}^{M \times L}, \quad (50)$$

where

$$\boldsymbol{\eta}_r = \left[\sqrt{P_T} \text{Re}\{\alpha_r\}, \sqrt{P_T} \text{Im}\{\alpha_r\}, \psi_r, \mu_r, \tau_r \right], \quad (51)$$

and

$$\mathbf{S}_r(\boldsymbol{\eta}_r) = \sqrt{P_T} \alpha_r \mathbf{A}(\mu_r, \psi_r, \delta_p, \nu_q) \mathbf{C}(\tau_r). \quad (52)$$

For the problem at hand, we choose the hidden data space as one noisy wavefront (path). After the expectation step, to find the estimate of the parameter vector $\hat{\boldsymbol{\eta}}_r$, the maximization step is performed.

In Appendix A, we derive new expressions for estimating the channel parameters, aiming to achieve maximum likelihood estimates of the parameters by solving one-dimensional problems iteratively. For notational convenience, we represent $\mathbf{A}(\mu_r, \psi_r, \delta_p, \nu_q)$ as $\mathbf{A}(\mu_r, \psi_r)$.

The delay $\hat{\tau}_r$ of the r th path can be estimated as

$$\hat{\tau}_r = \arg \max_{\tau_r} \left\{ \frac{\left| \text{tr} \left\{ \mathbf{C}^H(\tau_r) \mathbf{A}^H(\hat{\mu}_r, \hat{\psi}_r) \hat{\mathbf{X}}_r \right\} \right|^2}{\beta_r \sigma_n^2 \text{tr} \left\{ \mathbf{C}^H(\tau_r) \mathbf{A}^H(\hat{\mu}_r, \hat{\psi}_r) \mathbf{A}(\hat{\mu}_r, \hat{\psi}_r) \mathbf{C}(\tau_r) \right\}} \right\} \quad (53)$$

the spatial frequency $\hat{\mu}_r$ can be iteratively estimated as

$$\hat{\mu}_r = \arg \max_{\mu_r} \left\{ \frac{\left| \text{tr} \left\{ \mathbf{C}^H(\hat{\tau}_r) \mathbf{A}^H(\mu_r, \hat{\psi}_r) \hat{\mathbf{X}}_r \right\} \right|^2}{\beta_r \sigma_n^2 \text{tr} \left\{ \mathbf{C}^H(\hat{\tau}_r) \mathbf{A}^H(\mu_r, \hat{\psi}_r) \mathbf{A}(\mu_r, \hat{\psi}_r) \mathbf{C}(\hat{\tau}_r) \right\}} \right\}, \quad (54)$$

and the spatial frequency $\hat{\psi}_r$ can be iteratively estimated as

$$\hat{\psi}_r = \arg \max_{\psi_r} \left\{ \frac{\left| \text{tr} \left\{ \mathbf{C}^H(\hat{\tau}_r) \mathbf{A}^H(\hat{\mu}_r, \psi_r) \hat{\mathbf{X}}_r \right\} \right|^2}{\beta_r \sigma_n^2 \text{tr} \left\{ \mathbf{C}^H(\hat{\tau}_r) \mathbf{A}^H(\hat{\mu}_r, \psi_r) \mathbf{A}(\hat{\mu}_r, \psi_r) \mathbf{C}(\hat{\tau}_r) \right\}} \right\}. \quad (55)$$

Finally, the complex path gain $\sqrt{\hat{P}_T} \alpha_r$ can be analytically found as

$$\sqrt{\hat{P}_T} \alpha_r = \frac{\text{tr} \left\{ \mathbf{C}^H(\hat{\tau}_r) \mathbf{A}^H(\hat{\mu}_r, \hat{\psi}_r) \hat{\mathbf{X}}_r \right\}}{\text{tr} \left\{ \mathbf{C}^H(\hat{\tau}_r) \mathbf{A}^H(\hat{\mu}_r, \hat{\psi}_r) \mathbf{A}(\hat{\mu}_r, \hat{\psi}_r) \mathbf{C}(\hat{\tau}_r) \right\}}. \quad (56)$$

The expectation and maximization step are performed iteratively alternating between the paths until convergence.

A. Convergence Analysis of SAGE

The second stage of the high-resolution algorithm is to refine the coarse estimates achieved via modified PREIDG by the SAGE algorithm. To guarantee the convergence of the SAGE algorithm in a few iterations, it is mandatory to initialize it with estimates that are close to the global optimum. To this end, we use $\hat{\tau}_i$ (21), $\hat{\psi}_r$, $\hat{\mu}_r$ (31), and $\hat{\alpha}_r = 0$ to initialize the SAGE algorithm. One iteration of SAGE yields a full update of the parameter vector $\boldsymbol{\eta}$. The stopping thresholds used to declare the convergence are given by

$$\mathbf{T}_1 = \frac{|\hat{\psi}_{r_p} - \hat{\psi}_r|}{|\hat{\psi}_r|}, \quad (57)$$

$$T_2 = \frac{|\hat{\mu}_{r_p} - \hat{\mu}_r|}{|\hat{\mu}_r|}, \quad (58)$$

$$T_3 = \frac{|\hat{\tau}_{r_p} - \hat{\tau}_r|}{|\hat{\tau}_r|}, \quad (59)$$

$$T_4 = \frac{|\sqrt{\hat{P}_T} \alpha_{r_p} - \sqrt{\hat{P}_T} \alpha_r|}{|\sqrt{\hat{P}_T} \alpha_r|}, \quad (60)$$

where $\hat{\psi}_{r_p}, \hat{\mu}_{r_p}, \hat{\tau}_{r_p}, \sqrt{\hat{P}_T} \alpha_{r_p}$, are the previous estimates of spatial frequencies, time-delay, and complex path gain. Convergence of the SAGE algorithm is achieved if

$$\max \{T_1, T_2, T_3, T_4\} \leq \Gamma, \quad (61)$$

where Γ represents the stopping threshold.

B. Complexity of the Proposed Two-Step Approach

Recall that the proposed algorithm has two steps. In the first step, the modified PREIDG is proposed, where the received signal matrix \mathbf{Y} is filtered using the stored CAZAC sequence matrix $\mathbf{C}(0)$, as shown in (17), the complexity of which corresponds to that of the matrix product $\mathcal{O}(4M^2L)$. Regarding the complexity of LUT, which is computed offline only once with fixed size $D + 1$ and it can be used between any two beamforming vectors, and hence its contribution to complexity is negligible.

As far as the second step is concerned, which is the SAGE algorithm, the complexity involves the computation of $\hat{\tau}_r$ (53), $\hat{\mu}_r$ (54), $\hat{\psi}_r$ (55), and, $\hat{\alpha}_r$ (56). Summing up the number of operations defined by these equations, and assuming J iterations for the convergence, we arrive at $\mathcal{O}(4J(12M^2L + 8L^2M))$. The overall complexity is therefore $\mathcal{O}(4J(12M^2L + 8L^2M) + 4M^2L)$.

The complexity of another state-of-the-art ABP method depends on the vector multiplication, i.e., dot product between the channel steering vector $\mathbf{a}(\phi_r, \theta_r) \in \mathbb{C}^{M \times 1}$ and the beamforming vector $\mathbf{w}(\delta_p, \nu_q) \in \mathbb{C}^{M \times 1}$, which is given as $\mathcal{O}(4M)$. There are total number of M beam pairs, which leads to the total complexity of $\mathcal{O}(8M^2)$, respectively.

V. CRAMÉR-RAO LOWER BOUND (CRLB)

In this section, we derive the CRLB for the overall parameter vector of our problem, which comprises the spatial frequencies ψ_r, μ_r , complex path-gain $\sqrt{P_T} \alpha_r$ and the time-delay τ_r for each path, as given in (42). Assuming $\hat{\boldsymbol{\eta}}$ as an unbiased estimate of $\boldsymbol{\eta}$, the variance of the estimation error is lower-bounded by the diagonal elements of the inverse of the Fisher information matrix (FIM), $\mathbf{F}(\boldsymbol{\eta})$ [55]

$$\text{var}(\hat{\eta}_i) \geq [\mathbf{F}^{-1}(\boldsymbol{\eta})]_{ii}. \quad (63)$$

The lower bound of the standard deviation of the estimation error is given as

$$\sqrt{\text{CRLB}(\hat{\eta}_i)} = \sqrt{[\mathbf{F}^{-1}(\boldsymbol{\eta})]_{ii}}. \quad (64)$$

where, $\mathbf{F}(\boldsymbol{\eta})$ is given as [55],

$$[\mathbf{F}(\boldsymbol{\eta})]_{ij} = \frac{2}{\sigma_n^2} \text{Re} \left\{ \text{tr} \left\{ \frac{\partial \mathbf{S}^H(\boldsymbol{\eta})}{\partial \eta_i} \frac{\partial \mathbf{S}(\boldsymbol{\eta})}{\partial \eta_j} \right\} \right\}, \quad (65)$$

and $\mathbf{S}(\boldsymbol{\eta})$ is defined as,

$$\mathbf{S}(\boldsymbol{\eta}) = \sum_{r=1}^R \mathbf{S}(\boldsymbol{\eta}_r) = \sqrt{P_T} \sum_{r=1}^R \alpha_r \mathbf{A}(\mu_r, \psi_r) \mathbf{C}(\tau_r). \quad (66)$$

The FIM $\mathbf{F}(\boldsymbol{\eta})$ is given in (62), shown at the bottom of the page. The analytical expressions for the blocks of $\mathbf{F}(\boldsymbol{\eta})$ are derived in Appendix B.

VI. NUMERICAL RESULTS

In this section, the performance of the proposed modified PREIDG is compared to the state-of-the-art ABP algorithm [31] and the high-resolution parameter estimation is achieved via SAGE. The CRLB curves are also plotted as a reference. The transmitter at the BS is equipped with a PCAPS network architecture incorporated the BMs used for exciting the URA having $M = M_h M_v = 16$ and an inter-element spacing $d_h = d_v = \lambda/2$. We assume a carrier frequency $f_c = 28$ GHz and bandwidth $B = 200$ MHz, which results in a one symbol duration of $T_s = 5$ ns. We consider 1280 QPSK symbols as pilots for the estimation of the channel parameters. The channel parameters are modeled and chosen according to [56]. The LOS distance between the BS and UE is uniformly distributed in the two-dimensional range as,

$$X_{\text{los}} \sim \text{U}(30 \text{ m}, 60 \text{ m}), \quad (67)$$

and, the non-line-of-sight (NLOS) distances are uniformly distributed as

$$X_{\text{nlos}} = X_{\text{los}} + \Delta_{\text{nlos}}, \quad (68)$$

where Δ_{nlos} is the relative distance between the LOS and NLOS paths, modeled as $\Delta_{\text{nlos}} \sim \text{U}(4.5 \text{ m}, 24 \text{ m})$ which ends up with a delay difference between 3 and 16 symbols. We assume CAZAC sequences of length $L = 16$. Note that the length of the CAZAC sequence determines the maximum time-delay of the NLOS paths to be estimated. The path loss is given as

$$PL(\text{dB}) = 10\bar{n} \log_{10} \left(\frac{X}{X_0} \right), \quad (69)$$

$$\mathbf{F}(\boldsymbol{\eta}) = \begin{bmatrix} \mathbf{F}_{\text{Re}\{\boldsymbol{\alpha}\}\text{Re}\{\boldsymbol{\alpha}\}} & \mathbf{F}_{\text{Re}\{\boldsymbol{\alpha}\}\text{Im}\{\boldsymbol{\alpha}\}} & \mathbf{F}_{\text{Re}\{\boldsymbol{\alpha}\}\boldsymbol{\mu}} & \mathbf{F}_{\text{Re}\{\boldsymbol{\alpha}\}\boldsymbol{\psi}} & \mathbf{F}_{\text{Re}\{\boldsymbol{\alpha}\}\boldsymbol{\tau}} \\ \mathbf{F}_{\text{Re}\{\boldsymbol{\alpha}\}\text{Im}\{\boldsymbol{\alpha}\}}^T & \mathbf{F}_{\text{Im}\{\boldsymbol{\alpha}\}\text{Im}\{\boldsymbol{\alpha}\}} & \mathbf{F}_{\text{Im}\{\boldsymbol{\alpha}\}\boldsymbol{\mu}} & \mathbf{F}_{\text{Im}\{\boldsymbol{\alpha}\}\boldsymbol{\psi}} & \mathbf{F}_{\text{Im}\{\boldsymbol{\alpha}\}\boldsymbol{\tau}} \\ \mathbf{F}_{\text{Re}\{\boldsymbol{\alpha}\}\boldsymbol{\mu}}^T & \mathbf{F}_{\text{Im}\{\boldsymbol{\alpha}\}\boldsymbol{\mu}}^T & \mathbf{F}_{\boldsymbol{\mu}\boldsymbol{\mu}} & \mathbf{F}_{\boldsymbol{\mu}\boldsymbol{\psi}} & \mathbf{F}_{\boldsymbol{\mu}\boldsymbol{\tau}} \\ \mathbf{F}_{\text{Re}\{\boldsymbol{\alpha}\}\boldsymbol{\psi}}^T & \mathbf{F}_{\text{Im}\{\boldsymbol{\alpha}\}\boldsymbol{\psi}}^T & \mathbf{F}_{\boldsymbol{\mu}\boldsymbol{\psi}}^T & \mathbf{F}_{\boldsymbol{\psi}\boldsymbol{\psi}} & \mathbf{F}_{\boldsymbol{\psi}\boldsymbol{\tau}} \\ \mathbf{F}_{\text{Re}\{\boldsymbol{\alpha}\}\boldsymbol{\tau}}^T & \mathbf{F}_{\text{Im}\{\boldsymbol{\alpha}\}\boldsymbol{\tau}}^T & \mathbf{F}_{\boldsymbol{\mu}\boldsymbol{\tau}}^T & \mathbf{F}_{\boldsymbol{\psi}\boldsymbol{\tau}}^T & \mathbf{F}_{\boldsymbol{\tau}\boldsymbol{\tau}} \end{bmatrix}. \quad (62)$$

TABLE I
SIMULATION PARAMETERS

URA size (one-subarray)	$M_h M_v = 4 \times 4 = 16$
Inter-element spacing $d_h = d_v$	$\lambda/2$
AoD's azimuth generation (one sector of a cell)	$\phi_r^\circ \sim \mathcal{U}(-60^\circ, +60^\circ)$
AoD's elevation generation	$\theta_r^\circ \sim \mathcal{U}(90^\circ, 130^\circ)$
Carrier frequency f_c	28 GHz
Bandwidth	200 MHz
Symbol duration T_s	5 nsec
Number of users	1
Channel realizations	10000
Total pilot symbols used for all beams	1280 QPSK
Noise variance	$\sigma_n^2 = 1$
Number of subarrays used for estimation	$N_{RF} = 1$
Number of multipaths	$R = 3$

where \bar{n} represents the path loss exponent chosen as 2.1 and 2.4 for the LOS and NLOS components, respectively. X_0 is assumed as 1 m. γ_r is the magnitude of the complex path gain of the r th path and is defined as the ratio of the path loss for LOS (PL_{los}) and NLOS (PL_{nlos}) respectively. We are interested in the ratio of LOS and NLOS paths

$$\gamma_r = \sqrt{\frac{PL_{\text{los}}}{PL_{\text{nlos}}}}. \quad (70)$$

The complex path gain α_r for each path is given as

$$\frac{\alpha_r}{\alpha_1} = \gamma_r e^{j\varphi_r}, \quad (71)$$

where α_1 is the complex path gain for the LOS signal and is assumed as one, since only the ratio of the LOS path and NLOS paths does matter in a real scenario. φ_r is the phase of the complex path coefficient for each path and is generated as $\varphi_r \sim \mathcal{U}(0, 2\pi)$. Note that the phase of the complex gain φ_r is different for each sub-array at the BS while the magnitude γ_r is the same for each sub-array. In this approach, as the BS knows the geometry of the URA, it can estimate the phase of the other sub-arrays based on the estimation of the phase $\hat{\varphi}_1$ of the first sub-array. The AoDs azimuth ϕ_r and elevation θ_r for LOS and NLOS are generated assuming one sector of a cell as $\phi_r^\circ \sim \mathcal{U}(-60^\circ, +60^\circ)$ and $\theta_r^\circ \sim \mathcal{U}(90^\circ, 130^\circ)$, respectively. The noise variance is assumed as $\sigma_n^2 = 1$. The simulation parameters are summarized in Table I. The SNR is defined as

$$\text{SNR} = \frac{P_T |\alpha_1|^2}{\sigma_n^2}. \quad (72)$$

The RMSE for the different channel parameters defined as

$$\text{RMSE}(\hat{\phi}_r) = \sqrt{\mathbb{E} [|\phi_r - \hat{\phi}_r|^2]}, \quad (73)$$

$$\text{RMSE}(\hat{\theta}_r) = \sqrt{\mathbb{E} [|\theta_r - \hat{\theta}_r|^2]}, \quad (74)$$

$$\text{RMSE}(\sqrt{\hat{P}_T} \alpha_r) = \sqrt{\mathbb{E} \left[\left| \frac{\sqrt{P_T} \alpha_r - \sqrt{\hat{P}_T} \alpha_r}{\sqrt{P_T} \alpha_r} \right|^2 \right]}, \quad (75)$$

$$\text{RMSE}(\hat{\tau}_r) = \sqrt{\mathbb{E} [|\tau_r - \hat{\tau}_r|^2]}. \quad (76)$$

The CRLB on the error is calculated as

$$\sqrt{\text{CRLB}(\hat{\eta}_i)} = \sqrt{[\mathbf{F}^{-1}(\boldsymbol{\eta})]_{ii}}. \quad (77)$$

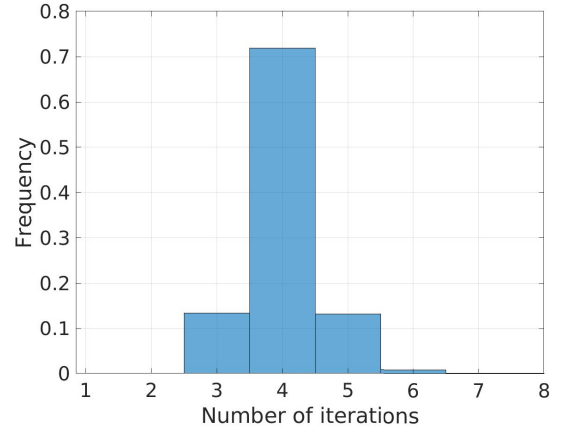


Fig. 5. Histogram showing the number of iterations, required for SAGE to converge.

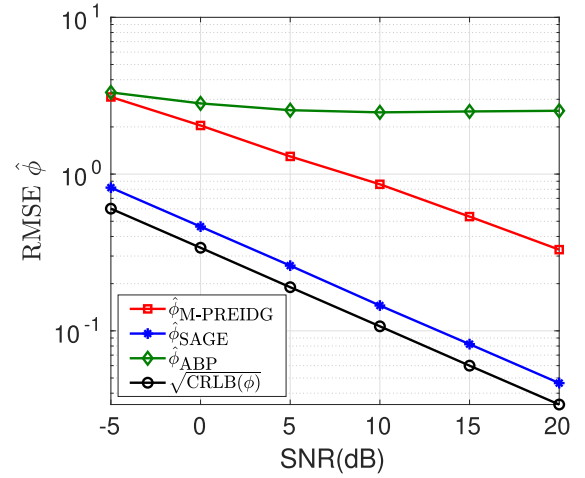


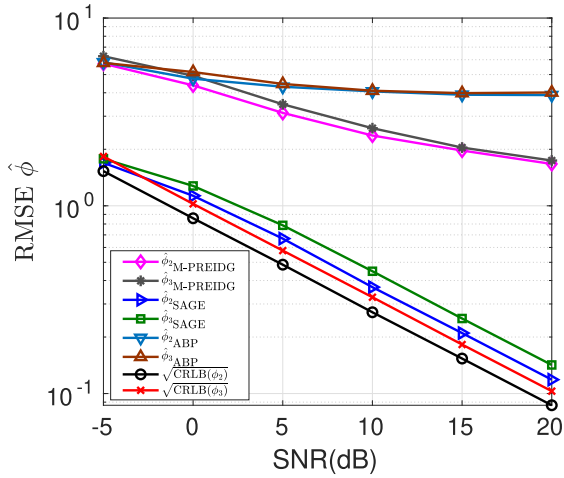
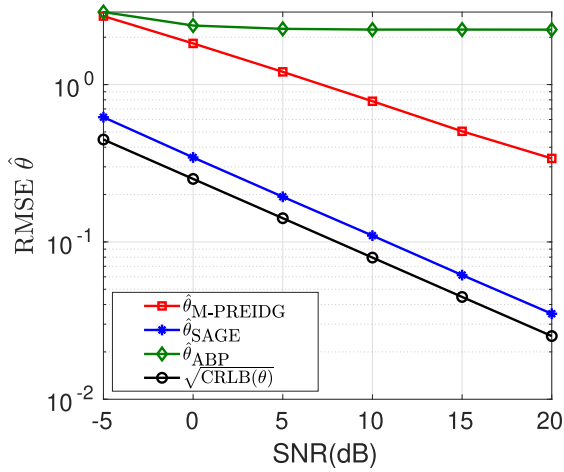
Fig. 6. RMSE of AoD azimuth (ϕ_r) for LOS path.

We assume 10000 channel realizations for calculating the RMSE for each parameter at each simulated SNR. Similarly, for the CRLB, each parameter is obtained by numerical averaging over 10000 realizations. The length of the LUT for the modified PREIDG algorithm is $D = 1001$.

To form beam pairs in the ABP method, we fix $\delta = \frac{2m\pi}{M_v} = \frac{\pi}{2}$, assuming $m = 1$ as explained in [31]. There are a total of 8 beam-pairs that can be formed for the estimation of ψ_r and μ_r . For the ABP method, *a priori* knowledge about the auxiliary beam-pair is assumed for the estimation of the spatial frequencies.

The motivation behind the modified-PREIDG based coarse estimation is to initialize the SAGE algorithm for getting the high-resolution parameter estimates with a reduced number of iterations for convergence to achieve the global optimum. We initialize the SAGE algorithm with $\hat{\psi}_r$, $\hat{\mu}_r$, $\hat{\tau}_i$ and assume $\sqrt{\hat{P}_T} \alpha_r = 0$, while fixing the threshold to $\Gamma = 10^{-3}$. The convergence of the SAGE algorithm is achieved within 6 iterations. We have noted that in 70% of the channel realizations, SAGE took only 4 iterations to converge, which is of practical interest as shown in Fig. 5.

Fig. 6 shows the performance of the proposed modified PREIDG algorithm as compared with the ABP method for

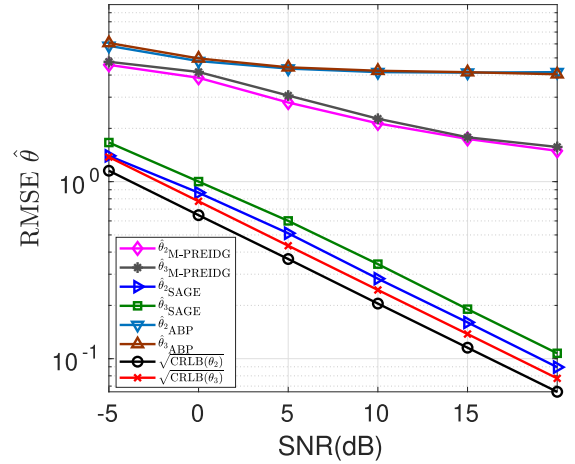
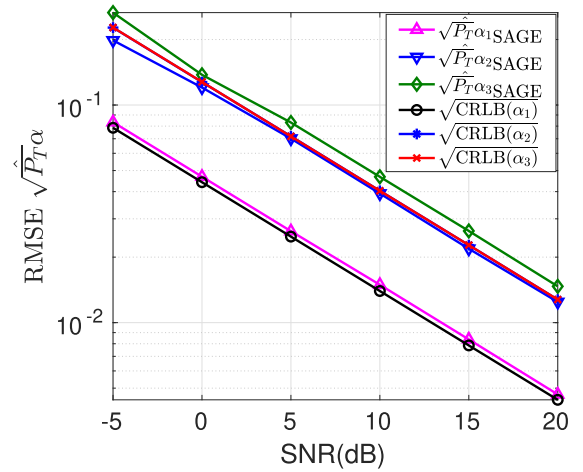
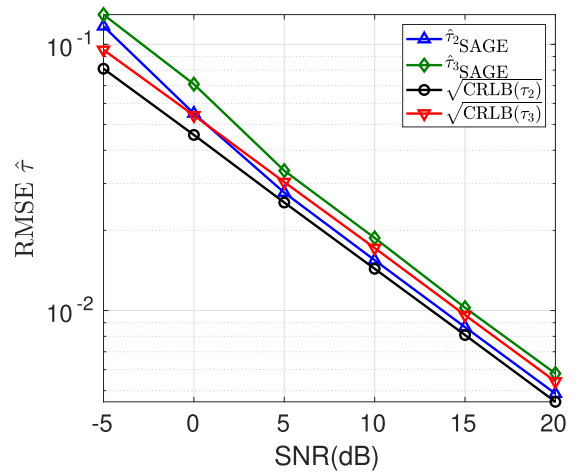

 Fig. 7. RMSE of AoD azimuth (ϕ_r) for NLOS paths.

 Fig. 8. RMSE of AoD elevation (θ_r) for LOS path.

the case of one LOS component. The modified PREIDG based parameter estimation yields a better performance as compared to the ABP method. Indeed, the latter does not show an improvement because of the limited number of beam pairs. The SAGE algorithm outperforms the ABP method due to its high-resolution capability. We can also note that the SAGE algorithm approaches the CRLB and thus proves to be efficient.

Fig. 7 shows the results for the NLOS scenario. We can see that the modified PREIDG algorithm shows good estimation performance as compared to the ABP method. The SAGE algorithm shows a better performance with less number of iterations as shown in Fig. 7. Furthermore, the SAGE algorithm approaches the CRLB closely.

In our next experiment, we evaluate performance of modified PREIDG against ABP for AoD elevation θ_r for LOS only as shown in Fig. 8. The proposed method shows a good performance as compared to the ABP. The SAGE estimation provides the best results, and nearly approaches the theoretical bound.

In Fig. 9, we show the results for elevation AoDs, considering the NLOS case. The proposed modified PREIDG shows an improved performance as compared to the ABP method.


 Fig. 9. RMSE of AoD azimuth (θ_r) for NLOS paths.

 Fig. 10. Performance of the SAGE algorithm for the estimation of the complex-path gain $\sqrt{P_T}\alpha_r$.

 Fig. 11. Performance of the SAGE algorithm for the estimation of the path delay τ_r .

Now, we consider the estimation of the path gains. We can see from Fig. 10 that the SAGE algorithm marked better performance for the estimation of the complex path gain ($\sqrt{P_T}\alpha_r$) and approaches the CRLB. The modified PREIDG and ABP method are unable to estimate the complex-path gains directly.

Fig. 11 depicts the RMSE of the estimates of the time delays. We can see that the SAGE algorithm provides estimates of the time-delay τ_r in high-resolution. The ABP algorithm is unable to estimate the time-delay τ_r , while the modified PREIDG can only estimate the integer delay. The initialization of the SAGE algorithm based on the coarse estimation achieved by the modified PREIDG enhances the estimation accuracy greatly with reasonable computational complexity.

VII. CONCLUSION

This paper proposed a novel strategy for high-resolution channel parameter estimation in mmWave systems using Butler matrices. The proposed approach has two steps. In the first step, a novel modified PREIDG parameter estimation algorithm is proposed based on only one fixed LUT for estimating both spatial frequencies, i.e., ψ_r, μ_r respectively. To decrease the computational complexity and get high-resolution channel parameter estimates, the SAGE algorithm is initialized with the coarse estimates achieved by modified PREIDG in the second step.

The channel is probed by the analog beams formed as the result of Kronecker product of two DFT matrices, which is energy efficiently implemented with the novel combination of Butler matrices in the analog domain to excite the URA. The proposed implementation removes the possibility of adaptive PSs in the analog domain by introducing fixed PSs.

The proposed combination of modified PREIDG and SAGE algorithms remarkably reduces the implementation complexity in the analog domain and improves the estimation accuracy, especially in the low SNR regime which is interesting for future cellular communication systems. Furthermore, we derived analytical expressions for the CRLB to assess the performance of the SAGE algorithm. We also compared the proposed modified PREIDG to the ABP algorithm, and our numerical results corroborate the improved azimuth and elevation RMSE performance of the proposed solution in both LOS and NLOS scenarios.

The proposed strategy can be further extended by multiple antennas at the UE for the estimation of the angle of arrival (AoA) and assuming dual-polarized antennas at the BS.

APPENDIX A

DERIVATION OF THE SAGE EXPRESSIONS FOR PARAMETER ESTIMATION

The cost function can written as

$$\hat{\boldsymbol{\eta}}_r = \arg \max_{\boldsymbol{\eta}_r} \left\{ \frac{1}{\beta_r \sigma_n^2} \left(\text{tr} \{ \mathbf{S}_r^H(\boldsymbol{\eta}_r) \hat{\mathbf{X}}_r \} + \text{tr} \{ \mathbf{S}_r^T(\boldsymbol{\eta}_r) \hat{\mathbf{X}}_r^* \} - \|\mathbf{S}_r(\boldsymbol{\eta}_r)\|_{\text{F}}^2 \right) \right\}, \quad (78)$$

where

$$\mathbf{S}_r(\boldsymbol{\eta}_r) = \sqrt{P_T} \alpha_r \mathbf{A}(\mu_r, \psi_r) \mathbf{C}(\tau_r), \quad (79)$$

and

$$\begin{aligned} \|\mathbf{S}_r(\boldsymbol{\eta}_r)\|_{\text{F}}^2 &= \text{tr} \{ \mathbf{S}_r^H(\boldsymbol{\eta}_r) \mathbf{S}_r(\boldsymbol{\eta}_r) \} \\ &= P_T \alpha_r \alpha_r^* \text{tr} \{ \mathbf{C}^H(\tau_r) \mathbf{A}^H(\mu_r, \psi_r) \mathbf{A}(\mu_r, \psi_r) \mathbf{C}(\tau_r) \}. \end{aligned} \quad (80)$$

Replacing (80) in (78), yields

$$\begin{aligned} \hat{\boldsymbol{\eta}}_r &= \arg \max_{\boldsymbol{\eta}_r} \left\{ \frac{1}{\beta_r \sigma_n^2} \left(\sqrt{P_T} \alpha_r^* \text{tr} \{ \mathbf{C}^H(\tau_r) \mathbf{A}^H(\mu_r, \psi_r) \hat{\mathbf{X}}_r \} \right. \right. \\ &\quad \left. \left. + \sqrt{P_T} \alpha_r \text{tr} \{ \mathbf{C}^T(\tau_r) \mathbf{A}^T(\mu_r, \psi_r) \hat{\mathbf{X}}_r^* \} \right. \right. \\ &\quad \left. \left. - P_T \alpha_r \alpha_r^* \text{tr} \{ \mathbf{C}^H(\tau_r) \mathbf{A}^H(\mu_r, \psi_r) \mathbf{A}(\mu_r, \psi_r) \mathbf{C}(\tau_r) \} \right) \right\} \\ &= \arg \max_{\boldsymbol{\eta}_r} \{ \boldsymbol{\Lambda}_r(\boldsymbol{\eta}_r) \}. \end{aligned} \quad (81)$$

To estimate α_r , we take the derivative of (81) with respect to $\sqrt{P_T} \alpha_r^*$ and equate it equal to zero, and we get

$$\sqrt{P_T} \alpha_r = \frac{\text{tr} \{ \mathbf{C}^H(\tau_r) \mathbf{A}^H(\mu_r, \psi_r) \hat{\mathbf{X}}_r \}}{\text{tr} \{ \mathbf{C}^H(\tau_r) \mathbf{A}^H(\mu_r, \psi_r) \mathbf{A}(\mu_r, \psi_r) \mathbf{C}(\tau_r) \}}. \quad (82)$$

To further solve for τ_r , μ_r and ψ_r , substituting (82) in (81) leads to

$$\begin{aligned} & \left(\hat{\tau}_r, \hat{\mu}_r, \hat{\psi}_r \right) \\ &= \arg \max_{\tau_r, \mu_r, \psi_r} \left\{ \frac{\left| \text{tr} \{ \mathbf{C}^H(\tau_r) \mathbf{A}^H(\mu_r, \psi_r) \hat{\mathbf{X}}_r \} \right|^2}{\beta_r \sigma_n^2 \text{tr} \{ \mathbf{C}^H(\tau_r) \mathbf{A}^H(\mu_r, \psi_r) \mathbf{A}(\mu_r, \psi_r) \mathbf{C}(\tau_r) \}} \right\}, \end{aligned} \quad (83)$$

which is used to iteratively and sequentially solve for $\hat{\tau}_r$, $\hat{\mu}_r$ and $\hat{\psi}_r$ in (53), (54) and (55).

APPENDIX B

ENTRIES OF THE FIM $\mathbf{F}(\boldsymbol{\eta})$

The entries of the block matrices of the FIM (62) are derived as,

$$\begin{aligned} & [\mathbf{F}_{\text{Re}\{\boldsymbol{\alpha}\}\text{Re}\{\boldsymbol{\alpha}\}}]_{ij} \\ &= \frac{P_T}{\sigma_n^2} 2 \text{Re} \left(\text{tr} \left\{ \sum_{r=1}^R \frac{\partial \alpha_r^*}{\partial \text{Re}\{\alpha_i\}} \mathbf{C}^H(\tau_r) \mathbf{A}^H(\mu_r, \psi_r) \right. \right. \\ &\quad \left. \left. \sum_{r=1}^R \frac{\partial \alpha_r}{\partial \text{Re}\{\alpha_j\}} \mathbf{A}(\mu_r, \psi_r) \mathbf{C}(\tau_r) \right\} \right), \end{aligned} \quad (84)$$

$$\begin{aligned} & [\mathbf{F}_{\text{Re}\{\boldsymbol{\alpha}\}\text{Im}\{\boldsymbol{\alpha}\}}]_{ij} \\ &= \frac{P_T}{\sigma_n^2} 2 \text{Re} \left(\text{tr} \left\{ \sum_{r=1}^R \frac{\partial \alpha_r^*}{\partial \text{Re}\{\alpha_i\}} \mathbf{C}^H(\tau_r) \mathbf{A}^H(\mu_r, \psi_r) \right. \right. \\ &\quad \left. \left. \sum_{r=1}^R \frac{\partial \alpha_r}{\partial \text{Im}\{\alpha_j\}} \mathbf{A}(\mu_r, \psi_r) \mathbf{C}(\tau_r) \right\} \right), \end{aligned} \quad (85)$$

$$\begin{aligned} & [\mathbf{F}_{\text{Re}\{\boldsymbol{\alpha}\}\boldsymbol{\mu}}]_{ij} \\ &= \frac{P_T}{\sigma_n^2} 2 \text{Re} \left(\text{tr} \left\{ \sum_{r=1}^R \frac{\partial \alpha_r^*}{\partial \text{Re}\{\alpha_i\}} \mathbf{C}^H(\tau_r) \mathbf{A}^H(\mu_r, \psi_r) \right. \right. \\ &\quad \left. \left. \sum_{r=1}^R \alpha_r \frac{\partial \mathbf{A}(\mu_r, \psi_r)}{\partial \mu_j} \mathbf{C}(\tau_r) \right\} \right), \end{aligned} \quad (86)$$

$$\begin{aligned} & [\mathbf{F}_{\text{Re}\{\boldsymbol{\alpha}\}\boldsymbol{\psi}}]_{ij} \\ &= \frac{P_T}{\sigma_n^2} 2 \text{Re} \left(\text{tr} \left\{ \sum_{r=1}^R \frac{\partial \alpha_r^*}{\partial \text{Re}\{\alpha_i\}} \mathbf{C}^H(\tau_r) \mathbf{A}^H(\mu_r, \psi_r) \right. \right. \\ &\quad \left. \left. \sum_{r=1}^R \alpha_r \frac{\partial \mathbf{A}(\mu_r, \psi_r)}{\partial \psi_j} \mathbf{C}(\tau_r) \right\} \right), \end{aligned} \quad (87)$$

$$\begin{aligned}
 & [\mathbf{F}_{\text{Re}\{\boldsymbol{\alpha}\}\boldsymbol{\tau}}]_{ij} \\
 &= \frac{P_T}{\sigma_n^2} 2\text{Re} \left(\text{tr} \left\{ \sum_{r=1}^R \frac{\partial \alpha_r^*}{\partial \text{Re}\{\alpha_i\}} \mathbf{C}^H(\tau_r) \right. \right. \\
 & \quad \left. \left. \mathbf{A}^H(\mu_r, \psi_r) \sum_{r=1}^R \alpha_r \mathbf{A}(\mu_r, \psi_r) \frac{\partial \mathbf{C}(\tau_r)}{\partial \tau_j} \right\} \right), \quad (88)
 \end{aligned}$$

$$\begin{aligned}
 & [\mathbf{F}_{\text{Im}\{\boldsymbol{\alpha}\}\text{Im}\{\boldsymbol{\alpha}\}}]_{ij} \\
 &= \frac{P_T}{\sigma_n^2} 2\text{Re} \left(\text{tr} \left\{ \sum_{r=1}^R \frac{\partial \alpha_r^*}{\partial \text{Im}\{\alpha_i\}} \mathbf{C}^H(\tau_r) \right. \right. \\
 & \quad \left. \left. \mathbf{A}^H(\mu_r, \psi_r) \sum_{r=1}^R \frac{\partial \alpha_r}{\partial \text{Im}\{\alpha_j\}} \mathbf{A}(\mu_r, \psi_r) \mathbf{C}(\tau_r) \right\} \right), \quad (89)
 \end{aligned}$$

$$\begin{aligned}
 & [\mathbf{F}_{\text{Im}\{\boldsymbol{\alpha}\}\boldsymbol{\mu}}]_{ij} \\
 &= \frac{P_T}{\sigma_n^2} 2\text{Re} \left(\text{tr} \left\{ \sum_{r=1}^R \frac{\partial \alpha_r^*}{\partial \text{Im}\{\alpha_i\}} \mathbf{C}^H(\tau_r) \mathbf{A}^H(\mu_r, \psi_r) \right. \right. \\
 & \quad \left. \left. \sum_{r=1}^R \alpha_r \frac{\partial \mathbf{A}(\mu_r, \psi_r)}{\partial \mu_j} \mathbf{C}(\tau_r) \right\} \right), \quad (90)
 \end{aligned}$$

$$\begin{aligned}
 & [\mathbf{F}_{\text{Im}\{\boldsymbol{\alpha}\}\boldsymbol{\psi}}]_{ij} \\
 &= \frac{P_T}{\sigma_n^2} 2\text{Re} \left(\text{tr} \left\{ \sum_{r=1}^R \frac{\partial \alpha_r^*}{\partial \text{Im}\{\alpha_i\}} \mathbf{C}^H(\tau_r) \mathbf{A}^H(\mu_r, \psi_r) \right. \right. \\
 & \quad \left. \left. \sum_{r=1}^R \alpha_r \frac{\partial \mathbf{A}(\mu_r, \psi_r)}{\partial \psi_j} \mathbf{C}(\tau_r) \right\} \right), \quad (91)
 \end{aligned}$$

$$\begin{aligned}
 & [\mathbf{F}_{\text{Im}\{\boldsymbol{\alpha}\}\boldsymbol{\tau}}]_{ij} \\
 &= \frac{P_T}{\sigma_n^2} 2\text{Re} \left(\text{tr} \left\{ \sum_{r=1}^R \frac{\partial \alpha_r^*}{\partial \text{Im}\{\alpha_i\}} \mathbf{C}^H(\tau_r) \mathbf{A}^H(\mu_r, \psi_r) \right. \right. \\
 & \quad \left. \left. \sum_{r=1}^R \alpha_r \mathbf{A}(\mu_r, \psi_r) \frac{\partial \mathbf{C}(\tau_r)}{\partial \tau_j} \right\} \right), \quad (92)
 \end{aligned}$$

$$\begin{aligned}
 & [\mathbf{F}_{\boldsymbol{\mu}\boldsymbol{\mu}}]_{ij} \\
 &= \frac{P_T}{\sigma_n^2} 2\text{Re} \left(\text{tr} \left\{ \sum_{r=1}^R \alpha_r^* \mathbf{C}^H(\tau_r) \frac{\partial \mathbf{A}^H(\mu_r, \psi_r)}{\partial \mu_i} \right. \right. \\
 & \quad \left. \left. \sum_{r=1}^R \alpha_r \frac{\mathbf{A}(\mu_r, \psi_r)}{\partial \mu_j} \mathbf{C}(\tau_r) \right\} \right), \quad (93)
 \end{aligned}$$

$$\begin{aligned}
 & [\mathbf{F}_{\boldsymbol{\mu}\boldsymbol{\psi}}]_{ij} \\
 &= \frac{P_T}{\sigma_n^2} 2\text{Re} \left(\text{tr} \left\{ \sum_{r=1}^R \alpha_r^* \mathbf{C}^H(\tau_r) \frac{\partial \mathbf{A}^H(\mu_r, \psi_r)}{\partial \mu_i} \right. \right. \\
 & \quad \left. \left. \sum_{r=1}^R \alpha_r \frac{\mathbf{A}(\mu_r, \psi_r)}{\partial \psi_j} \mathbf{C}(\tau_r) \right\} \right), \quad (94)
 \end{aligned}$$

$$\begin{aligned}
 & [\mathbf{F}_{\boldsymbol{\mu}\boldsymbol{\tau}}]_{ij} \\
 &= \frac{P_T}{\sigma_n^2} 2\text{Re} \left(\text{tr} \left\{ \sum_{r=1}^R \alpha_r^* \mathbf{C}^H(\tau_r) \frac{\partial \mathbf{A}^H(\mu_r, \psi_r)}{\partial \mu_i} \right. \right. \\
 & \quad \left. \left. \sum_{r=1}^R \alpha_r \mathbf{A}(\mu_r, \psi_r) \frac{\partial \mathbf{C}(\tau_r)}{\partial \tau_j} \right\} \right), \quad (95)
 \end{aligned}$$

$$\begin{aligned}
 & [\mathbf{F}_{\boldsymbol{\psi}\boldsymbol{\psi}}]_{ij} \\
 &= \frac{P_T}{\sigma_n^2} 2\text{Re} \left(\text{tr} \left\{ \sum_{r=1}^R \alpha_r^* \mathbf{C}^H(\tau_r) \frac{\partial \mathbf{A}^H(\mu_r, \psi_r)}{\partial \psi_i} \right. \right. \\
 & \quad \left. \left. \sum_{r=1}^R \alpha_r \frac{\mathbf{A}(\mu_r, \psi_r)}{\partial \psi_j} \mathbf{C}(\tau_r) \right\} \right), \quad (96)
 \end{aligned}$$

$$\begin{aligned}
 & [\mathbf{F}_{\boldsymbol{\psi}\boldsymbol{\tau}}]_{ij} \\
 &= \frac{P_T}{\sigma_n^2} 2\text{Re} \left(\text{tr} \left\{ \sum_{r=1}^R \alpha_r^* \mathbf{C}^H(\tau_r) \frac{\partial \mathbf{A}^H(\mu_r, \psi_r)}{\partial \psi_i} \right. \right. \\
 & \quad \left. \left. \sum_{r=1}^R \alpha_r \mathbf{A}(\mu_r, \psi_r) \frac{\partial \mathbf{C}(\tau_r)}{\partial \tau_j} \right\} \right), \quad (97)
 \end{aligned}$$

$$\begin{aligned}
 & [\mathbf{F}_{\boldsymbol{\tau}\boldsymbol{\tau}}]_{ij} \\
 &= \frac{P_T}{\sigma_n^2} 2\text{Re} \left(\text{tr} \left\{ \sum_{r=1}^R \alpha_r^* \frac{\partial \mathbf{C}^H(\tau_r)}{\partial \tau_i} \mathbf{A}^H(\mu_r, \psi_r) \right. \right. \\
 & \quad \left. \left. \sum_{r=1}^R \alpha_r \mathbf{A}(\mu_r, \psi_r) \frac{\partial \mathbf{C}(\tau_r)}{\partial \tau_j} \right\} \right). \quad (98)
 \end{aligned}$$

The partial derivative of α_r and α_r^* is calculated as

$$\frac{\partial \alpha_r}{\partial \text{Re}\{\alpha_i\}} = \frac{\partial \alpha_r^*}{\partial \text{Re}\{\alpha_i\}} = \begin{cases} 1 & \text{if } (r = i) \\ 0 & \text{if } (r \neq i), \end{cases} \quad (99)$$

$$\frac{\partial \alpha_r}{\partial \text{Im}\{\alpha_i\}} = -\frac{\partial \alpha_r^*}{\partial \text{Im}\{\alpha_i\}} = \begin{cases} j & \text{if } (r = i) \\ 0 & \text{if } (r \neq i). \end{cases} \quad (100)$$

Given that

$$a_m(\mu_r, \psi_r) = e^{-j[(p-1)\mu_r + (q-1)\psi_r]}, \quad (101)$$

where $m = q + (p-1)M_v$, $p \in \{1, \dots, M_h\}$, $q \in \{1, \dots, M_v\}$ and $M = M_h M_v$, the partial derivative of $\mathbf{A}(\mu_r, \psi_r)$ is calculated as:

$$\frac{\partial \mathbf{A}(\mu_r, \psi_r)}{\partial \mu_r} = \text{diag}\{\mathbf{a}_h^H(\mu_r, \psi_r) \mathbf{w}_m(\delta_p, \nu_q)\}_{m=1}^{M=M_h M_v}, \quad (102)$$

and

$$\frac{\partial \mathbf{A}(\mu_r, \psi_r)}{\partial \psi_r} = \text{diag}\{\mathbf{a}_v^H(\mu_r, \psi_r) \mathbf{w}_m(\delta_p, \nu_q)\}_{m=1}^{M=M_h M_v}. \quad (103)$$

where following (101)

$$\mathbf{a}'_h(\mu_r, \psi_r) = \frac{\partial \mathbf{a}(\mu_r, \psi_r)}{\partial \mu_r} = \{-j(p-1) a_m(\mu_r, \psi_r)\}_{m=1}^{M_h M_v}, \quad (104)$$

and

$$\mathbf{a}'_v(\mu_r, \psi_r) = \frac{\partial \mathbf{a}(\mu_r, \psi_r)}{\partial \psi_r} = \{-j(q-1) a_m(\mu_r, \psi_r)\}_{m=1}^{M_h M_v}. \quad (105)$$

The sequence can be given as

$$c(t) = \sum_{n=-\infty}^{+\infty} c(n) h(t - nT_s), \quad (106)$$

where $h(t)$ is the raised cosine (RC) pulse

$$h(t) = \frac{\sin\left(\pi \frac{t}{T_s}\right) \cos\left(\rho\pi \frac{t}{T_s}\right)}{\pi \frac{t}{T_s} \sqrt{1 - \left(2\rho \frac{t}{T_s}\right)^2}}, \quad (107)$$

and $\rho \in [0, 1]$, represents the roll-off factor. The delayed sequence by τ_r is represented as

$$c(t - \tau_r) = \sum_{n=-\infty}^{+\infty} c(n)h(t - nT_s - \tau_r). \quad (108)$$

The partial derivative with respect to τ_r can be written as

$$\begin{aligned} \frac{\partial c(t - \tau_r)}{\partial \tau_r} &= \sum_{n=-\infty}^{+\infty} c(n) \frac{\partial h(t - nT_s - \tau_r)}{\partial \tau_r} \\ &= - \sum_{n=-\infty}^{+\infty} \left(c(n) \frac{\partial h(\tilde{t})}{\partial \tilde{t}} \bigg|_{\tilde{t}=t-nT_s-\tau_r} \right). \quad (109) \end{aligned}$$

REFERENCES

- [1] Z. Pi and F. Khan, "An introduction to millimeter-wave mobile broadband systems," *IEEE Commun. Mag.*, vol. 49, no. 6, pp. 101–107, Jun. 2011.
- [2] T. S. Rappaport *et al.*, "Millimeter wave mobile communications for 5G cellular: It will work!" *IEEE Access*, vol. 1, pp. 335–349, 2013.
- [3] F. Rusek, D. Persson, B. Kiong Lau, E. G. Larsson, T. L. Marzetta, and F. Tufvesson, "Scaling up MIMO: Opportunities and challenges with very large arrays," *IEEE Signal Process. Mag.*, vol. 30, no. 1, pp. 40–60, Jan. 2013.
- [4] J. Mo and R. W. Heath, "Capacity analysis of one-bit quantized MIMO systems with transmitter channel state information," *IEEE Trans. Signal Process.*, vol. 63, no. 20, pp. 5498–5512, Oct. 2015.
- [5] A. Mezghani and J. A. Nossek, "Analysis of Rayleigh-fading channels with 1-bit quantized output," in *Proc. IEEE Int. Symp. Inf. Theory*, Jul. 2008, pp. 260–264.
- [6] A. Mezghani and J. A. Nossek, "On ultra-wideband MIMO systems with 1-bit quantized outputs: Performance analysis and input optimization," in *Proc. IEEE Int. Symp. Inf. Theory*, Jun. 2007, pp. 1286–1289.
- [7] C.-S. Lee and W.-H. Chung, "Hybrid RF-baseband precoding for cooperative multiuser massive MIMO systems with limited RF chains," *IEEE Trans. Commun.*, vol. 65, no. 4, pp. 1575–1589, Apr. 2017.
- [8] J. Zhu, W. Xu, and N. Wang, "Secure massive MIMO systems with limited RF chains," *IEEE Trans. Veh. Technol.*, vol. 66, no. 6, pp. 5455–5460, Jun. 2017.
- [9] L. Yang, Y. Zeng, and R. Zhang, "Efficient channel estimation for millimeter wave MIMO with limited RF chains," in *Proc. IEEE Int. Conf. Commun. (ICC)*, May 2016, pp. 1–6.
- [10] L. Lian, A. Liu, and V. K. N. Lau, "Optimal-tuned weighted LASSO for massive MIMO channel estimation with limited RF chains," in *Proc. IEEE Global Commun. Conf. (GLOBECOM)*, Dec. 2017, pp. 1–6.
- [11] F. Asim, J. Nossek, F. Antreich, C. C. Cavalcante, and A. L. F. D. Almeida, "Maximum likelihood channel estimation for millimeter-wave MIMO systems with hybrid beamforming," in *Proc. 23rd Int. ITG Workshop Smart Antennas (WSA)*, Apr. 2019, pp. 1–6.
- [12] F. Asim, F. Antreich, C. C. Cavalcante, A. de Almeida, and J. A. Nossek, "Channel parameter estimation for millimeter-wave cellular systems with hybrid beamforming," *Signal Process.*, vol. 176, pp. 2619–2692, Jul. 2020.
- [13] W. F. Moulder, W. Khalil, and J. L. Volakis, "60-GHz two-dimensionally scanning array employing wideband planar switched beam network," *IEEE Antennas Wireless Propag. Lett.*, vol. 9, pp. 818–821, 2010.
- [14] X. Wang, M. Laabs, D. Plettemeier, K. Kosaka, and Y. Matsunaga, "MIMO antenna array system with integrated 16×16 butler matrix and power amplifiers for 28 GHz wireless communication," in *Proc. 12th German Microw. Conf. (GeMiC)*, Mar. 2019, pp. 127–130.
- [15] X. Wang *et al.*, "28 GHz multi-beam antenna array based on wideband high-dimension 16×16 butler matrix," in *Proc. IEEE Int. Symp. Antennas Propag. USNC/URSI Nat. Radio Sci. Meeting*, Jul. 2018, pp. 1–4.
- [16] Y. Han, S. Jin, J. Zhang, J. Zhang, and K.-K. Wong, "DFT-based hybrid beamforming multiuser systems: Rate analysis and beam selection," *IEEE J. Sel. Topics Signal Process.*, vol. 12, no. 3, pp. 514–528, Jun. 2018.
- [17] J. Rodriguez-Fernandez, N. Gonzalez-Prelcic, K. Venugopal, and R. W. Heath, "Frequency-domain compressive channel estimation for frequency-selective hybrid millimeter wave MIMO systems," *IEEE Trans. Wireless Commun.*, vol. 17, no. 5, pp. 2946–2960, May 2018.
- [18] B. Wang, F. Gao, S. Jin, H. Lin, and G. Y. Li, "Spatial- and frequency-wideband effects in millimeter-wave massive MIMO systems," *IEEE Trans. Signal Process.*, vol. 66, no. 13, pp. 3393–3406, Jul. 2018.
- [19] B. Wang *et al.*, "Spatial-wideband effect in massive MIMO with application in mmWave systems," *IEEE Commun. Mag.*, vol. 56, no. 12, pp. 134–141, Dec. 2018.
- [20] A. C. Gurbuz, Y. Yapici, and I. Guvenc, "Sparse channel estimation in millimeter-wave communications via parameter perturbed OMP," in *Proc. IEEE Int. Conf. Commun. Workshops (ICC Workshops)*, May 2018, pp. 1–6.
- [21] K. He, Y. Li, and C. Yin, "A novel CS-based non-orthogonal multiple access MIMO system for downlink of MTC in 5G," in *Proc. IEEE 28th Annu. Int. Symp. Pers., Indoor, Mobile Radio Commun. (PIMRC)*, Oct. 2017, pp. 1–5.
- [22] P. Wang, M. Pajovic, P. V. Orlik, T. Koike-Akino, K. J. Kim, and J. Fang, "Sparse channel estimation in millimeter wave communications: Exploiting joint AoD-AoA angular spread," in *Proc. IEEE Int. Conf. Commun. (ICC)*, May 2017, pp. 1–6.
- [23] Y. C. Eldar, P. Kuppinger, and H. Bolcskei, "Block-sparse signals: Uncertainty relations and efficient recovery," *IEEE Trans. Signal Process.*, vol. 58, no. 6, pp. 3042–3054, Jun. 2010.
- [24] A. Alkhateeb, O. El Ayach, G. Leus, and R. W. Heath, "Channel estimation and hybrid precoding for millimeter wave cellular systems," *IEEE J. Sel. Topics Signal Process.*, vol. 8, no. 5, pp. 831–846, Oct. 2014.
- [25] J. Lee, G.-T. Gil, and Y. H. Lee, "Channel estimation via orthogonal matching pursuit for hybrid MIMO systems in millimeter wave communications," *IEEE Trans. Commun.*, vol. 64, no. 6, pp. 2370–2386, Jun. 2016.
- [26] K. Venugopal, A. Alkhateeb, N. Gonzalez Prelcic, and R. W. Heath, "Channel estimation for hybrid architecture-based wideband millimeter wave systems," *IEEE J. Sel. Areas Commun.*, vol. 35, no. 9, pp. 1996–2009, Sep. 2017.
- [27] A. Shahmansoori, G. E. Garcia, G. Destino, G. Seco-Granados, and H. Wymeersch, "Position and orientation estimation through millimeter-wave MIMO in 5G systems," *IEEE Trans. Wireless Commun.*, vol. 17, no. 3, pp. 1822–1835, Mar. 2018.
- [28] D. Zhu, J. Choi, and R. W. Heath, "Auxiliary beam pair design in mmWave cellular systems with hybrid precoding and limited feedback," in *Proc. IEEE Int. Conf. Acoust., Speech Signal Process. (ICASSP)*, Mar. 2016, pp. 3391–3395.
- [29] D. Zhu, J. Choi, and R. W. Heath, "Auxiliary beam pair enabled AoD and AoA estimation in mmWave FD-MIMO systems," in *Proc. IEEE Global Commun. Conf. (GLOBECOM)*, Dec. 2016, pp. 1–6.
- [30] D. Zhu, J. Choi, and R. W. Heath, "Auxiliary beam pair enabled AoD and AoA estimation in closed-loop large-scale millimeter-wave MIMO systems," *IEEE Trans. Wireless Commun.*, vol. 16, no. 7, pp. 4770–4785, Jul. 2017.
- [31] D. Zhu, J. Choi, and R. W. Heath, "Two-dimensional AoD and AoA acquisition for wideband millimeter-wave systems with dual-polarized MIMO," *IEEE Trans. Wireless Commun.*, vol. 16, no. 12, pp. 7890–7905, Dec. 2017.
- [32] J. Singh and S. Ramakrishna, "On the feasibility of codebook-based beamforming in millimeter wave systems with multiple antenna arrays," *IEEE Trans. Wireless Commun.*, vol. 14, no. 5, pp. 2670–2683, May 2015.
- [33] C. Hu, L. Dai, T. Mir, Z. Gao, and J. Fang, "Super-resolution channel estimation for mmWave massive MIMO with hybrid precoding," *IEEE Trans. Veh. Technol.*, vol. 67, no. 9, pp. 8954–8958, Sep. 2018.
- [34] W. Ma, C. Qi, and G. Y. Li, "High-resolution channel estimation for frequency-selective mmWave massive MIMO systems," *IEEE Trans. Wireless Commun.*, vol. 19, no. 5, pp. 3517–3529, May 2020.
- [35] G. Sommerkom, D. Hampicke, R. Klukas, A. Richter, A. Schneider, and R. Thoma, "Reduction of DoA estimation errors caused by antenna array imperfections," in *Proc. 29th Eur. Microw. Conf.*, Oct. 1999, pp. 287–290.
- [36] M. Eberhardt, P. Eschlwech, and E. Biebl, "Investigations on antenna array calibration algorithms for direction-of-arrival estimation," *Adv. Radio Sci.*, vol. 14, pp. 181–190, Sep. 2016. [Online]. Available: <https://www.adv-radio-sci.net/14/181/2016/>

- [37] K. Xiong, Z. Liu, and W. Jiang, "SAGE-based algorithm for direction-of-arrival estimation and array calibration," *Int. J. Antennas Propag.*, vol. 2014, pp. 1–8, 2014.
- [38] R. Feng, Y. Liu, J. Huang, J. Sun, and C.-X. Wang, "Comparison of music, unitary ESPRIT, and SAGE algorithms for estimating 3D angles in wireless channels," in *Proc. IEEE/CIC Int. Conf. Commun. China (ICCC)*, Oct. 2017, pp. 1–6.
- [39] R. Feng, Y. Liu, J. Huang, J. Sun, C.-X. Wang, and G. Goussetis, "Wireless channel parameter estimation algorithms: Recent advances and future challenges," *China Commun.*, vol. 15, no. 5, pp. 211–228, May 2018.
- [40] F. A. de Leon and J. J. S. Marciano, "Application of MUSIC, ESPRIT and SAGE algorithms for narrowband signal detection and localization," in *Proc. IEEE Region 10 Conf. (TENCON)*, 2006, pp. 1–4.
- [41] X. Yin and B. H. Fleury, "Nominal direction and direction spread estimation for slightly distributed scatterers using the SAGE algorithm," in *Proc. IEEE 61st Veh. Technol. Conf.*, vol. 1, May 2005, pp. 25–29.
- [42] J. Zhang and M. Haardt, "Channel estimation for hybrid multi-carrier mmwave MIMO systems using three-dimensional unitary esprit in DFT beamspace," in *Proc. IEEE 7th Int. Workshop Comput. Adv. Multi-Sensor Adapt. Process. (CAMSAP)*, Dec. 2017, pp. 1–5.
- [43] J. Chen, X. Ge, and Q. Ni, "Coverage and handoff analysis of 5G fractal small cell networks," *IEEE Trans. Wireless Commun.*, vol. 18, no. 2, pp. 1263–1276, Feb. 2019.
- [44] A. Liao, Z. Gao, H. Wang, S. Chen, M.-S. Alouini, and H. Yin, "Closed-loop sparse channel estimation for wideband millimeter-wave full-dimensional MIMO systems," *IEEE Trans. Commun.*, vol. 67, no. 12, pp. 8329–8345, Dec. 2019.
- [45] Z. Zhou, J. Fang, L. Yang, H. Li, Z. Chen, and R. S. Blum, "Low-rank tensor decomposition-aided channel estimation for millimeter wave MIMO-OFDM systems," *IEEE J. Sel. Areas Commun.*, vol. 35, no. 7, pp. 1524–1538, Jul. 2017.
- [46] W. Huang, Y. Huang, Y. Zeng, and L. Yang, "Wideband millimeter wave communication with lens antenna array: Joint beamforming and antenna selection with group sparse optimization," *IEEE Trans. Wireless Commun.*, vol. 17, no. 10, pp. 6575–6589, Oct. 2018.
- [47] Z. Wan, Z. Gao, B. Shim, K. Yang, G. Mao, and M.-S. Alouini, "Compressive sensing based channel estimation for millimeter-wave full-dimensional MIMO with lens-array," *IEEE Trans. Veh. Technol.*, vol. 69, no. 2, pp. 2337–2342, Feb. 2020.
- [48] A. Garcia-Rodriguez, V. Venkateswaran, P. Rulikowski, and C. Masouros, "Hybrid analog-digital precoding revisited under realistic RF modeling," *IEEE Wireless Commun. Lett.*, vol. 5, no. 5, pp. 528–531, Oct. 2016.
- [49] R. L. Frank and S. A. Zadoff, "Phase shift pulse codes with good periodic correlation properties (correspondence)," *IRE Trans. Inf. Theory*, vol. 8, pp. 381–382, Oct. 1962.
- [50] B. M. Popovic, "Generalized chirp-like polyphase sequences with optimum correlation properties," *IEEE Trans. Inf. Theory*, vol. 38, no. 4, pp. 1406–1409, Jul. 1992.
- [51] U. H. Rohrs and L. P. Linde, "Some unique properties and applications of perfect squares minimum phase CAZAC sequences," in *Proc. South Afr. Symp. Commun. Signal Process.*, 1992, pp. 155–160.
- [52] M. Tschudin, C. Brunner, T. Kurpjuhn, M. Haardt, and J. A. Nossek, "Comparison between unitary ESPRIT and SAGE for 3-D channel sounding," in *Proc. IEEE 49th Veh. Technol. Conf.*, vol. 2, May 1999, pp. 1324–1329.
- [53] J. A. Fessler and A. O. Hero, "Space-alternating generalized expectation-maximization algorithm," *IEEE Trans. Signal Process.*, vol. 42, no. 10, pp. 2664–2677, Oct. 1994.
- [54] B. H. Fleury, M. Tschudin, R. Heddergott, D. Dahlhaus, and K. Ingeman Pedersen, "Channel parameter estimation in mobile radio environments using the SAGE algorithm," *IEEE J. Sel. Areas Commun.*, vol. 17, no. 3, pp. 434–450, Mar. 1999.
- [55] S. M. Kay, *Fundamentals of Statistical Signal Processing: Estimation Theory*. New York, NY, USA: Prentice-Hall, 2010.
- [56] M. K. Samimi and T. S. Rappaport, "3-D millimeter-wave statistical channel model for 5G wireless system design," *IEEE Trans. Microw. Theory Techn.*, vol. 64, no. 7, pp. 2207–2225, Jul. 2016.



Fazal-E-Asim (Member, IEEE) received the bachelor's degree in telecommunication engineering from the University of Engineering and Technology, Peshawar, Pakistan, in 2010, the master's degree in electrical engineering from the Institute of Space Technology, Islamabad, Pakistan, in 2014, and the Ph.D. degree in teleinformatics engineering from the Federal University of Ceará, Brazil, in 2020. His general areas of interest includes signal processing for wireless communications.



Felix Antreich (Senior Member, IEEE) received the Diploma degree in electrical engineering and the Doktor-Ingenieur (Ph.D.) degree from the Technical University of Munich (TUM), Munich, Germany, in 2003 and 2011, respectively.

From 2003 to 2016, he was an Associate Researcher with the Department of Navigation, Institute of Communications and Navigation, German Aerospace Center (DLR), Wessling, Germany. From 2016 to 2018, he was a Visiting Professor with the Department of Teleinformatics Engineering (DETI), Federal University of Ceará (UFC), Fortaleza, Brazil. Since July 2018, he has been a Professor with the Division of Electronics Engineering, Department of Telecommunications, Aeronautics Institute of Technology (ITA), São José dos Campos, Brazil. His research interests include sensor array signal processing for global navigation satellite systems (GNSS) and wireless communications, estimation theory, wireless sensor networks, positioning, localization, and signal design for synchronization. He has received the VDE Award 2011 for an outstanding dissertation from Verband der Elektrotechnik Elektronik Informationstechnik e.V. (VDE), Germany, in November 2011, as well as the Best Presentation Award at the ION GNSS 2012, ION GNSS 2015, and ION GNSS+ 2020 conferences in September 2012, 2015, and 2020, respectively. From 2014 to 2016, he was a Special Visiting Researcher (PVE) at the University of Brasilia (UnB), within the Programa Ciencia sem Fronteiras funded by the Coordenação de Aperfeiçoamento de Pessoal de Nível Superior (CAPES) and the Conselho Nacional de Desenvolvimento Científico e Tecnológico (CNPq).



Charles C. Cavalcante (Senior Member, IEEE) received the B.Sc. and M.Sc. degrees in electrical engineering from the Federal University of Ceará (UFC), Brazil, in 1999 and 2001, respectively, and the Ph.D. degree from the University of Campinas (UNICAMP), Brazil, in 2004. He received grants for Scientific and Technological Development (from 2004 to 2007) and for Scientific Research Productivity from the Brazilian Research Council (CNPq) (since March 2009). He is currently an Associate Professor with the Teleinformatics Engineering Department, UFC, holding the Statistical Signal Processing Chair. From August 2014 to July 2015, he was a Visiting Assistant Professor with the Department of Computer Science and Electrical Engineering (CSEE), University of Maryland Baltimore County (UMBC), USA. He has been working on signal processing strategies for communications, where he has several papers published in journal and conferences, has authored three international patents, and has worked on several funded research projects on the signal processing and wireless communications areas. He is also a coauthor of the book "Unsupervised Signal Processing: Channel Equalization and Source Separation" (CRC Press) and a co-editor of the book "Signals and Images: Advances and Results in Speech, Estimation, Compression, Recognition, Filtering, and Processing" (CRC Press). He is also a Researcher of the Wireless Telecommunications Research Group (GTel), where he leads research on signal processing and wireless communications. His main research interests include signal processing for communications, statistical signal processing, and information geometry. He is a Senior Member of the Brazilian Telecommunications Society (SBrT). He was the President of the Brazilian Telecommunication Society (SBrT) for the term 2018–2020, and he is the IEEE Signal Processing Society Regional Director-at-Large for Regions 7 & 9 for the term 2020–2021.



André L. F. de Almeida (Senior Member, IEEE) received the double Ph.D. degree in sciences and teleinformatics engineering from the University of Nice Sophia Antipolis, France, and the Federal University of Ceará, Fortaleza, Brazil, in 2007. He is currently an Associate Professor with the Department of Teleinformatics Engineering, Federal University of Ceará. He has held multiple visiting professor positions at the University of Nice Sophia-Antipolis, France (2012, 2013, 2015, 2018, and 2019). He has published over 70 refereed journal

articles, 130 conference papers, and six book chapters. His research interests include the topics of channel estimation, sensor array processing, and multiantenna systems. An important part of his research has been devoted to multilinear algebra and tensor decompositions with applications to communications and signal processing. He is a member of the Sensor Array and Multichannel (SAM) Technical Committee of the IEEE Signal Processing Society (SPS) and of the EURASIP Signal Processing for Multi-Sensor Systems Technical Area Committee (SPMuS-TAC). He is a Research Fellow of the Brazilian National Council for Scientific and Technological Development (CNPq). In January 2018, he was elected as an Affiliate Member of the Brazilian Academy of Sciences. He was the General Co-Chair of the IEEE CAMSAP'2017 workshop and served as the Technical Co-Chair of the Symposium on "Tensor Methods for Signal Processing and Machine Learning" at IEEE GlobalSIP 2018 and IEEE GlobalSIP 2019. He also served as the Technical Co-Chair of the IEEE SAM 2020 workshop, Hangzhou, China. He is also the General Co-Chair of the IEEE CAMSAP 2021 workshop, Costa Rica. He has been a technical committee member and a reviewer for several flagship signal processing conferences (e.g. IEEE SAM, IEEE CAMSAP, EUSIPCO, and IEEE ICASSP) and has organized several invited special sessions in these conferences.



Josef A. Nossek (Life Fellow, IEEE) received the Dipl.-Ing. and Dr. techn. degrees in electrical engineering from the Vienna University of Technology, Austria, in 1974 and 1980, respectively. In 1974, he joined Siemens AG, Munich, Germany, as a member of technical staff, became supervisor in 1978, and was the Head of Department in 1980. In 1987, he was promoted to be Head of all radio systems design. Since 1989, he has been a Full Professor of Circuit Theory and Signal Processing at the Munich University of Technology, where he

teaches undergraduate and graduate courses on circuit and systems theory and signal processing and leads research on signal processing algorithms for communications, especially multiantenna systems. From 2016 to 2019, he was a Full Professor at the Federal University of Ceará, Brazil. He was the Elected President, President, and Past President of the IEEE Circuits and Systems Society in 2001, 2002, and 2003, respectively. He was the Vice President of VDE (Verband der Elektrotechnik, Elektronik und Informationstechnik e.V.) from 2005–2010. His awards include the ITG Best Paper Award 1988, the Mannesmann Mobilfunk (now Vodafone) Innovationsaward 1998, and the Award for Excellence in Teaching from the Bavarian Ministry for Science, Research and Art in 1998. He received the Golden Jubilee Medal for "Outstanding Contributions to the Society" and the Education Award from the IEEE Circuits and Systems Society in 1999 and 2008, respectively. In 2008, he also received the Order of Merit of the Federal Republic of Germany, and he has been an Elected Member of the German National Academy of Engineering Sciences (acatech) in 2009. He received an Honorary Doctorate in 2013 and the Ring of Honor from VDE in 2014.